From travelling waves to mild chaos: a supercritical bifurcation cascade in pipe flow

F. Mellibovsky and B. Eckhardt

Link to this article: http://journals.cambridge.org/abstract_S0022112012003266

How to cite this article:
F. Mellibovsky and B. Eckhardt (2012). From travelling waves to mild chaos: a supercritical bifurcation cascade in pipe flow. Journal of Fluid Mechanics, 709, pp 149-190 doi:10.1017/jfm.2012.326

Request Permissions : Click here

From travelling waves to mild chaos: a supercritical bifurcation cascade in pipe flow

F. Mellibovsky[1]† and B. Eckhardt[2,3]

[1] Departament de Física Aplicada, Universitat Politècnica de Catalunya, 08034, Barcelona, Spain

[2] Fachbereich Physik, Philipps-Universität Marburg, D-35032 Marburg, Germany

[3] J.M. Burgerscentrum, Delft University of Technology, 2638 CD Delft, The Netherlands

We study numerically a succession of transitions in pipe Poiseuille flow that lead from simple travelling waves to waves with chaotic time-dependence. The waves at the origin of the bifurcation cascade are twofold azimuthally periodic, shift–reflect symmetric, and have a non-dimensional axial wavelength of 1.927 diameters. As the Reynolds number is increased, successive transitions result in a wide range of time-dependent solutions that include spiralling, modulated travelling, modulated spiralling, doubly modulated spiralling and mildly chaotic waves. Numerical evidence suggests that the latter spring from heteroclinic tangles of the stable and unstable invariant manifolds of two shift–reflect symmetric, modulated travelling waves. The chaotic set thus produced is confined to a limited range of Reynolds numbers, bounded by the occurrence of manifold tangencies. The subspace of discrete symmetry to which the states studied here belong makes many of the bifurcation and path-following investigations presented readily accessible. However, we expect that most of the phenomenology carries over to the full state space, thus suggesting a mechanism for the formation and break-up of invariant states that can give rise to chaotic dynamics.

Key words: bifurcation, chaos, transition to turbulence

---

1. Introduction

The problem of the transition to turbulence in shear flows is one of great theoretical complexity and paramount practical relevance (Grossmann 2000; Eckhardt *et al.* 2007; Eckhardt 2009). Since Osborne Reynolds (1883) published his fundamental work on the onset of turbulent motion in a straight pipe of circular cross-section, this problem has become a paradigm for this class of flows. Many theoretical (Boberg & Brosa 1988; Brosa & Grossmann 1999), numerical (Schmid & Henningson 1994; Zikanov 1996; Shan *et al.* 1999) and experimental (Wygnanski & Champagne 1973; Wygnanski, Sokolov & Friedman 1975; Darbyshire & Mullin 1995) studies have focused on elucidating how turbulence can appear for finite-amplitude perturbations despite the linear stability of the laminar Hagen–Poiseuille flow (Pfenniger 1961; Meseguer & Trefethen 2003). Lifetime studies have shown that pipe flow turbulence is transient (Hof *et al.* 2006; Avila, Willis & Hof 2010) and that the eventual decay to laminar flow is a local memoryless process. The fact that turbulence is persistent at sufficiently

† Email address for correspondence: fmellibovsky@fa.upc.edu

high Reynolds numbers has recently been ascribed to its invasive nature, which causes laminar gaps to be quickly filled by adjacent expanding turbulent domains (Avila *et al.* 2011).

The computation of finite-amplitude solutions in the form of travelling waves (Faisst & Eckhardt 2003; Wedin & Kerswell 2004; Pringle & Kerswell 2007; Eckhardt *et al.* 2008) has opened up a window for further studies from a nonlinear dynamics perspective. This parallels similar developments in other flows such as plane Couette flow (Nagata 1997; Wang, Gibson & Waleffe 2007) or plane Poiseuille (Pugh & Saffman 1988; Ehrenstein & Koch 1991; Soibelman & Meiron 1991). These waves typically appear in saddle-node bifurcations and come in a variety of symmetries (Faisst & Eckhardt 2003; Pringle & Kerswell 2007; Pringle, Duguet & Kerswell 2009). The upper-branch solutions, with wall friction coefficients close to turbulent values, seem to play a role in developed turbulence and have been observed in experiments (Hof *et al.* 2004; Eckhardt *et al.* 2007; Kerswell & Tutty 2007; Schneider, Eckhardt & Vollmer 2007; Willis & Kerswell 2008). Their lower-branch counterparts appear to be connected to the critical threshold separating the basins of attraction of laminar and turbulent flows, and are relevant for the transition process (Skufca, Yorke & Eckhardt 2006; Schneider, Eckhardt & Yorke 2007; Duguet, Willis & Kerswell 2008; Mellibovsky & Meseguer 2009). Some of the latest developments for the case of pipe flow are compiled in Eckhardt (2009).

The presence of finite-amplitude persistent structures is a prerequisite for the appearance of turbulence, but further structural information is needed to explain or understand the dynamics. Specifically, further bifurcations are needed in order to increase the temporal complexity and to change the nature of the dynamics from persistent to transient, a salient feature of short-pipe turbulence. Identifying the phase space structures that govern transition and turbulence may ultimately lead to the development of efficient strategies for turbulence control. These strategies could then be exploited in applications that would benefit from drag reduction. Accordingly, we focus here on the transitions of these waves in order to explore the origins of the increasing complexity observed in pipe flow.

Since tracking of complex states with several unstable directions in high-dimensional spaces is possible (Sanchez, Net & Simo 2010) but technically difficult and computationally demanding, we focus on the subspace with twofold azimuthal periodicity that was also explored in Mellibovsky & Eckhardt (2011), henceforth referred to as ME11. The symmetry eliminates some unstable directions so that a direct identification of the relevant structures without the need for advanced tracking or stabilization methods is possible. Specifically, we have identified a family of states in this subspace for which the lower-branch solutions have a single unstable direction within the subspace so that a symmetry-restricted time-evolution converges when combined with edge-tracking techniques (Skufca *et al.* 2006; Schneider *et al.* 2007; Duguet *et al.* 2008; Schneider & Eckhardt 2009). When parametrized in terms of axial wavenumber (κ) and Reynolds number (Re), this family of waves appears in a Takens–Bogdanov bifurcation, thoroughly studied in ME11. The analysis showed that for wavenumbers beyond a certain value, upper-branch waves are stable within the subspace and therefore within the grasp of direct time-evolution. Here we will study the evolution of the upper branch solutions and their secondary instabilities that lead to time-dependent behaviour and, eventually, to chaos.

Due to the broken fore–aft symmetry of pipe flow, the simplest possible solutions already exhibit time-dependence in the form of an axial downstream drift with a constant speed. Some spiralling (rotating-travelling) waves, which rotate due to the
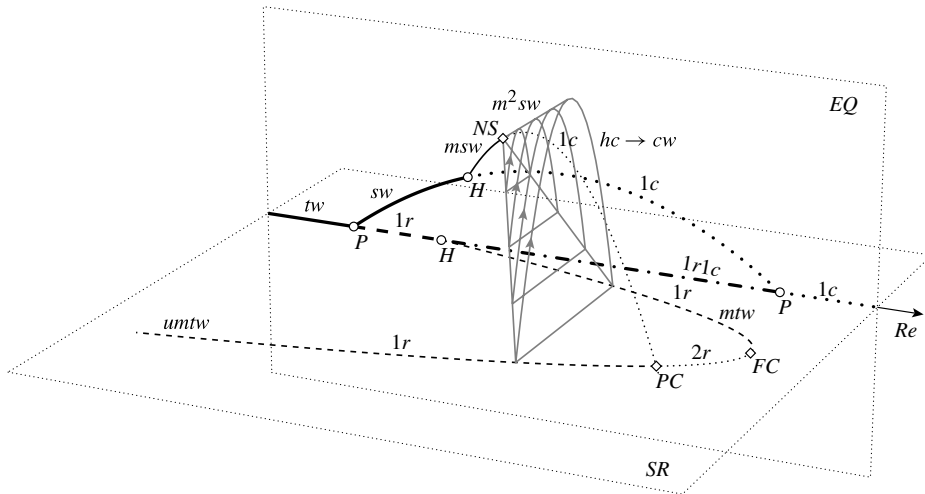
FIGURE 1. Sketch summarizing the bifurcation structure identified for $\kappa = 1.63$ and discussed in the present manuscript. The three axes indicate the Reynolds number (*Re*, the control parameter), the departure from the space of relative equilibria (*EQ* vertical plane) and the departure from the shift–reflect subspace (horizontal *SR* plane). The various states found are travelling (*tw*), spiralling (*sw*), modulated travelling (*mtw*), unstable modulated travelling (*umtw*), modulated spiralling (*msw*), doubly modulated spiralling (*m²sw*) and chaotic (*cw*) waves. Pitchfork (*P*), Hopf (*H*), Neimark–Sacker (*NS*), fold-of-cycles (*FC*), pitchfork-of-cycles (*PC*), and a global heteroclinic-cyclic (*hc*) bifurcations are indicated. Solid, dashed, dotted and dash-dotted lines represent solutions with zero-dimensional (stable), one-, two- and three-dimensional unstable manifolds. Real and complex pairs are indicated by *r* and *c*.

breach of all azimuthal reflection (Z_2) symmetries, have also been identified (Pringle & Kerswell 2007; Mellibovsky & Meseguer 2009). Travelling and spiralling waves are relative equilibria. Their time-dependence does not result from true dynamics, but from a mere drift along the group orbit. Duguet, Pringle & Kerswell (2008) took time-dependence in pipe flow one step further by computing a branch of modulated travelling waves. A second family arose naturally from the study of the Takens–Bogdanov bifurcation in ME11, but again its existence seemed at best incidental. No further solutions of higher complexity that bridge the gap between the steady laminar flow and turbulence have been observed or computed in pipe flow, although evidence of a chaos-inducing homoclinic tangle has recently been reported in plane-Couette flow (van Veen & Kawahara 2011).

The aim of this study is precisely to take advantage of the stability of upper-branch waves in the family of shift–reflect symmetric states to explore a bifurcating cascade and to produce, along the way, an array of solutions exhibiting ever-increasing time-dependent complexity. Figure 1 summarizes in a sketch the bifurcation cascade that the travelling waves undergo as *Re* is increased. All relative equilibria (*EQ* vertical plane) as well as all stable states (solid lines) and part of the shift–reflect (*SR* horizontal plane) unstable states are readily accessible and give evidence of the bifurcation scenario proposed. As the figure shows schematically, successive destabilization of a branch of travelling waves (*tw*) results in two independent branches of spiralling (*sw*) and modulated travelling (*mtw*) waves. The spiralling waves sequentially lose stability to modulated spiralling (*msw*) and doubly modulated spiralling (*m²sw*) waves, which grow and collide in a heteroclinic-cyclic connection with the modulated travelling

waves. We will argue that, at the final stage, the clean heteroclinic-cyclic bifurcation sketched in the figure is replaced by a wedge of manifold tangencies giving rise to mildly chaotic waves (as defined and explained in §5).

The states discussed here may be stable in their symmetry-restricted subspace, but they are typically unstable when considered within the full state space. Since there is nothing to suggest that the bifurcation sequence observed and discussed here requires the symmetry restriction (except for reducing the effort that has to go into their identification), it can be expected that it also appears for travelling waves in the full state space. In this sense the present study also suggests paths for the formation and break-up of other invariant structures in pipe flow.

The outline of the paper is as follows. In §2, we present the pipe Poiseuille flow problem and sketch a numerical scheme for the integration of the resulting equations. The symmetries of the problem are discussed and numerical methods for the computation and stability analysis of relative equilibria are briefly summarized. Some aspects of bifurcation theory in the case of relative equilibria are also reviewed in §2. A detailed exploration of parameter space delimiting the region of existence of relevant travelling and spiralling waves and an analysis of their stability is presented in §3 and extended in appendices A and B. In §4 we discuss successive transitions from these waves into increasingly complex types of solutions and describe their main features. The detailed aspects of the global transition leading to the creation of a chaotic set are then discussed in §5. Conclusions and further remarks are summarized in §6.

2. Formulation and methods

In this section we briefly summarize the methods section from a previous contribution so that the symbols and key elements are introduced. Further details can be found in §2 of ME11.

We consider the flow of an incompressible Newtonian fluid through a pipe of circular cross-section at constant mass flow. The Reynolds number $Re = UD/\nu$ is based on the mean axial flow speed U, the pipe diameter D and the kinematic viscosity ν. The base profile, in non-dimensional cylindrical coordinates $\boldsymbol{x} = (r, \theta, z)$, is $\boldsymbol{u}_b = u_r^b \hat{\boldsymbol{r}} + u_\theta^b \hat{\boldsymbol{\theta}} + u_z^b \hat{\boldsymbol{z}} = (1 - r^2) \hat{\boldsymbol{z}}$. The equations for the perturbations in velocity $\boldsymbol{u} = (u_r, u_\theta, u_z)$ and pressure p are the Navier–Stokes equations

$$\partial_t \boldsymbol{u} = -\nabla p + \frac{1}{Re} \Delta \boldsymbol{u} - (\boldsymbol{u} \cdot \nabla)(\boldsymbol{u}_b + \boldsymbol{u}) - (\boldsymbol{u}_b \cdot \nabla)\boldsymbol{u} + f \hat{\boldsymbol{z}}, \qquad (2.1)$$

together with the incompressibility constraint,

$$\nabla \cdot \boldsymbol{u} = 0, \qquad (2.2)$$

the condition for constant mass flux,

$$Q(\boldsymbol{u}) = \int_0^{2\pi} \int_0^1 (\boldsymbol{u} \cdot \hat{\boldsymbol{z}}) \, r \, \mathrm{d}r \, \mathrm{d}\theta = 0, \qquad (2.3)$$

and the boundary conditions,

$$\boldsymbol{u}(1, \theta, z; t) = \boldsymbol{0}, \quad \boldsymbol{u}(r, \theta + 2\pi/n_s, z, t) = \boldsymbol{u}(r, \theta, z + 2\pi/\kappa, t) = \boldsymbol{u}(r, \theta, z, t). \quad (2.4)$$

The adjustable axial forcing $f = f(t)$ in (2.1) ensures the constant mass flux constraint (2.3). In addition to the no-slip boundary condition at the wall we have periodicity in the azimuthal and axial directions. In the azimuthal direction we

take $n_s = 2$ throughout, confining the analysis to twofold azimuthally periodic fields. All solutions in this subspace are also solutions to the full Navier–Stokes equations, but the imposed discrete symmetry suppresses some undesired unstable directions. The axial wavenumber κ is taken as an additional parameter. We focus here on the value $\kappa = 1.63$ ($\Lambda \simeq 1.927D$), for which the bifurcation cascade presents its maximum complexity and richness of solutions, but extend the analysis to the interval $\kappa \in [1.5, 1.7]$ for further explorations presented in appendix A. The Reynolds number is varied in the range $Re \in [1800, 2800]$, with most of the bifurcations concentrated in a small range around $Re \simeq 2200$.

For the spatial discretization of (2.1)–(2.4) we use a solenoidal spectral Petrov–Galerkin scheme thoroughly described and tested by Meseguer & Mellibovsky (2007). The velocity field is expanded in the form

$$\boldsymbol{u}(r, \theta, z; t) = \sum_{l=-L}^{L} \sum_{n=-N}^{N} e^{-i(\kappa lz + n_s n\theta)} \, \boldsymbol{u}_{ln}(r; t), \qquad (2.5)$$

$$\boldsymbol{u}_{ln}(r; t) = \sum_{m=0}^{M} \sum_{i=1,2} a_{lnm}^{(i)}(t) \, \boldsymbol{v}_{lnm}^{(i)}(r), \qquad (2.6)$$

with $a_{lnm}^{(i)}$ the complex expansion coefficients which are collected in a state vector $\boldsymbol{a}$. The spectral resolution, checked as adequate for the computations performed in this study, has been set to $L = 16$, $N = 12$ and $M = 36$, corresponding to ± 16 axial and ± 12 azimuthal Fourier modes, and to 37 Chebyshev collocation points for the radial coordinate. For the time-evolution, we take a fourth-order linearly implicit method with stepsize $\Delta t = 1 \times 10^{-2} D/(4U)$.

Fluid flow solutions lie in infinite-dimensional space, of which we compute finite, yet high-dimensional representations. Elegant approaches to project these solutions onto low-dimensional spaces to aid visualization have been devised (Gibson, Halcrow & Cvitanović 2008) and successfully applied to other flows such as plane Couette (Gibson, Halcrow & Cvitanović 2009). We take the simpler approach of using some suitable expansion coefficients and global derived quantities to represent the flow. To free the representation from the drifting degeneracy associated to the travelling and/or rotating component of the waves, it is more convenient to use the absolute value rather than the coefficients themselves. In this study we will be making extensive use of the moduli of a streamwise independent ($|a_{010}^{(2)}|$), an axisymmetric ($|a_{100}^{(2)}|$) and a mixed ($|a_{110}^{(2)}|$) coefficient. In what follows, the absolute value symbols will be omitted for simplicity.

The basic solutions come in the form of travelling waves. Travelling and spiralling waves are relative equilibria that possess the continuous space–time symmetry

$$(u, v, w)_{tw}(r, \theta, z; t) = (u, v, w)_{tw}(r, \theta - c_\theta t, z - c_z t; 0), \qquad (2.7)$$

where c_z is the axial drift speed and c_θ is the azimuthal drift speed, which is exactly zero for non-rotating travelling waves. In a co-moving reference frame travelling downstream with speed c_z, travelling waves appear as stationary solutions. Near a relative equilibrium the drift dynamics is trivial and decouples from the dynamics orthogonal to the drift. As a result, bifurcations of relative equilibria can be analysed in two steps, first describing the bifurcations associated to the orthogonal dynamics, then adding the corresponding drift along the travelling direction (Krupa 1990). Thus, the bifurcation analysis of travelling waves can be carried out analogously to that

of fixed points, as long as special care is taken in the neighbourhood of homoclinic connections (Rand 1982; Golubitsky, LeBlanc & Melbourne 2000).

Relative or degenerate equilibria and solutions bifurcating from them have a pure frequency associated to the advection speed (solid-body translation/rotation). Time-series of local quantities such as point velocities or pressures are necessarily imprinted by this frequency, but the modulation disappears by restating the problem in a co-moving frame. In order to avoid the transformation to this co-moving frame of reference, it is convenient to have observables that are translationally/rotationally invariant in the axial/azimuthal directions: then the drifting motion of the travelling/rotating wave drops out and they appear as fixed points in this observable without further action. Global quantities such as modal energies or volume-averaged fields naturally overlook solid-body rotation and translation, making them suitable for a decoupled analysis in the direction orthogonal to the degenerate drift. One such quantity is the normalized energy,

$$\varepsilon(\boldsymbol{u}) = \frac{1}{2\epsilon_b} \int_0^{2\pi/\kappa} \mathrm{d}z \int_0^{2\pi} \mathrm{d}\theta \int_0^1 r\,\mathrm{d}r\,\boldsymbol{u}^* \cdot \boldsymbol{u}, \qquad (2.8)$$

with $\epsilon_b = \pi^2/(3\kappa)$ the energy of the basic flow and * symbolizing complex conjugation. This energy decouples exactly into the sum of its axial/azimuthal Fourier components $\varepsilon_{ln} = \varepsilon(\boldsymbol{u}_{ln})$. As a measure of three-dimensional structure, we define the non-axisymmetric streamwise dependent component as $\varepsilon_{3D} = \sum_{l,n\neq 0}\varepsilon(\boldsymbol{u}_{ln})$.

Another such quantity is the mean axial pressure gradient needed to drive the flow at constant mass flux, normalized by the pressure gradient for the corresponding laminar flow,

$$(\boldsymbol{\nabla}p)_z = \left\langle \iint_{r,\theta} \frac{\partial p}{\partial z} \right\rangle_z \Bigg/ \left(\frac{\mathrm{d}p}{\mathrm{d}z} \right)_{lam} = 1 + \frac{Re\,f}{4}. \qquad (2.9)$$

It is closely related to the wall friction factor (Schlichting & Gersten 2000):

$$C_f = \frac{2D}{\rho U^2} \left\langle \iint_{r,\theta} \frac{\partial p}{\partial z} \right\rangle_z = 64\frac{(\boldsymbol{\nabla}p)_z}{Re}, \qquad (2.10)$$

which constitutes a good indicator of whether the flow is laminar or turbulent.

In the azimuthal direction, all the solutions studied here are invariant under the cyclic group C_2 (rotations by integer multiples of π). Besides this symmetry, the travelling wave family that constitutes the departing point for the present study possesses an additional discrete symmetry: a combined shift–reflect symmetry. Solutions invariant under this symmetry operation,

$$S\boldsymbol{u}(\boldsymbol{x}) = S(u, v, w)(r, \theta_i + \theta, z; t) = (u, -v, w)(r, \theta_i - \theta, z + \pi/\kappa; t), \qquad (2.11)$$

are left unaltered when shifted half a wavelength downstream and then reflected with respect to any of two diametral planes tilted with $\theta_i = \theta_0$ and $\theta_0 + \pi/2$, where θ_0 parametrizes the azimuthal degeneracy of solutions. It can be shown that the expansion coefficient $a_{100}^{(2)}$ vanishes exactly when this symmetry is present, its norm giving a fairly good notion of how far apart from the symmetry space any given flow field is. The S symmetry is a remnant version of the Z_2 reflections group implied by the broken $O(2) = SO(2) \rtimes Z_2$ azimuthal symmetry. Waves that break all left–right symmetries incorporate an azimuthal precessing motion on top of the axial drift, so that they spiral and the azimuthal drift speed c_θ in (2.7) ceases to be zero. Evidently,

the decoupling from the drift dynamics of the drift-orthogonal dynamics discussed for travelling waves holds true for waves that also rotate.

Modulated waves arise from Hopf bifurcations of travelling and spiralling waves. They obey a different type of space–time symmetry:

$$(u, v, w)_{mw}(r, \theta, z; t + T) = (u, v, w)_{mw}(r, \theta - \bar{c}_\theta\, T, z - \bar{c}_z\, T; t), \qquad (2.12)$$

where T is the period of the modulation and $\bar{c}_z$ and $\bar{c}_\theta$ are average drift speeds. No general result is available when it comes to their stability. The effects on the degenerate frequency (or frequencies) associated to the travelling (or spiralling) component of the wave when a modulational frequency comes into play cannot be discarded at once. Nonetheless, as our computations will show, the approach of choosing an appropriate co-moving frame of reference remains accurate, and modulated travelling (spiralling) waves seem to behave as relative periodic orbits rather than as generic quasiperiodic orbits on a 2-torus (3-torus).

In order to choose this appropriate frame of reference we define the instantaneous axial and azimuthal drift speeds as the values c_z and c_θ, respectively, that minimize, at any given instant of time, the 2-norm of the state vector's rate of change:

$$\arg\min_{c_z, c_\theta} \left\| \lim_{\delta t \to 0} \left[\frac{\boldsymbol{a}(t + \delta t) - \boldsymbol{T}(c_z \delta t)\boldsymbol{R}(c_\theta \delta t)\, \boldsymbol{a}(t)}{\delta t} \right] \right\|, \qquad (2.13)$$

where $\arg\min$ returns the values of the parameters for which the minimum of the function is obtained. $\boldsymbol{T}(\Delta z)$ and $\boldsymbol{R}(\Delta\theta)$ are the diagonal operators for translation and rotation, whose action on the components of the state vector is defined by

$$\left. \begin{aligned} (\boldsymbol{T}(\Delta z)\, \boldsymbol{a})_{lnm}^{(i)} &= a_{lnm}^{(i)}\, \mathrm{e}^{-\mathrm{i}\kappa l \Delta z}, \\ (\boldsymbol{R}(\Delta\theta)\, \boldsymbol{a})_{lnm}^{(i)} &= a_{lnm}^{(i)}\, \mathrm{e}^{-\mathrm{i}n_s n \Delta\theta}. \end{aligned} \right\} \qquad (2.14)$$

Strictly speaking, a limiting process making $\delta t \to 0$ should be applied. In practice, using the integration time step is a sufficiently good approximation.

Therefore, we will systematically work on a co-moving reference frame in which waves become equilibria and we will apply continuous dynamical systems theory. Moreover, modulated and doubly modulated waves become periodic orbits and 2-tori, so that they can be seen as equilibria and periodic orbits, respectively, on a purposely designed drift-invariant Poincaré section. This is accomplished by using drift-independent quantities upon definition of the Poincaré section. The stability of modulated waves can then be studied through their associated Poincaré map, making use of discrete-time dynamical systems theory.

Besides the complications introduced by the bifurcation of relative equilibria, i.e. group orbits invariant under the flow of equivariant vector fields, we will be dealing here with additional symmetries that modify or replace well-known bifurcating scenarios that are typical of low-dimensional dynamical systems. To overcome this, we will take advantage of the substantial developments that have been achieved in the last two decades regarding bifurcation in dynamical systems with symmetries (Golubitsky, Stewart & Schaeffer 1988; Crawford & Knobloch 1991; Chossat & Lauterbach 2000).

3. Relative equilibria

The relative equilibria considered here are travelling waves or spiralling waves, and were first computed by Faisst & Eckhardt (2003) and Wedin & Kerswell (2004) using volume forcing homotopy. Their existence extends in Reynolds number to as low
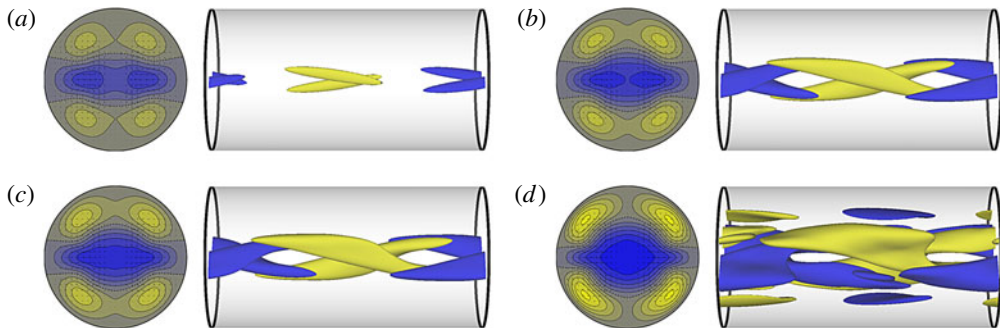
FIGURE 2. (Colour online) Travelling waves at $(\kappa, Re) = (1.63, 2215)$. On the left of each subfigure are z-averaged cross-sectional axial velocity contours spaced at intervals of $\Delta \langle u_z \rangle_z = 0.1U$. In-plane velocity vectors are also displayed. On the right of each subfigure are axial vorticity isosurfaces at $\omega_z = \pm 1U/D$. Fluid flows rightwards. Blue (dark grey) for negative, yellow (light) for positive. (*a*) Lower-branch (tw_0); (*b*) lower-middle-branch (tw); (*c*) upper-middle-branch (tw_2); and (*d*) upper-branch (tw_3) travelling waves.

as $Re \simeq 1358.5$ for the optimal wavenumber $\kappa \simeq 1.55$ (Faisst & Eckhardt 2003; Wedin & Kerswell 2004).

In what follows, we continue both upper- and lower-branch members of this family of travelling waves to higher Re and analyse their stability in order to explore the framework in which increasingly complex dynamics occur. We do so using the continuation scheme, the Newton solver and the stability analysis tools described and used in ME11. While we focus here on $\kappa = 1.63$, the analysis is extended to varying κ in appendix A.

We do not study the shift–reflect mirror-symmetric family of travelling waves (Duguet *et al.* 2008) that coexists in state space with the solutions discussed here. They reside in a region of phase space that is noticeably far from the present region of interest and there are no indications that they interact with the solutions found in this work, at least not for the parameter ranges studied here.

3.1. *Travelling waves*

Lower-branch travelling waves of this family can be continued to extremely high Re without much noticeable change to their stability properties, regardless of κ. Like many other lower-branch travelling waves, they seem to develop a critical layer as Re is increased (Viswanath 2009) and exhibit a single unstable eigenmode when considered in the azimuthal subspace they inhabit. They are edge states (Schneider *et al.* 2007) of the twofold azimuthally periodic pipe within this subspace. In the full state space they may be part of the edge and may provide the symmetric states needed to connect the stable manifolds of non-symmetric but symmetry-related edge states (Vollmer, Schneider & Eckhardt 2009). Figure 2(*a*) shows z-averaged cross-sectional axial velocity contours ($\langle u_z \rangle_z$, left) and a couple of axial vorticity isosurfaces (ω_z, right) of a lower-branch travelling wave at $(\kappa, Re) = (1.63, 2215)$. The shift–reflect symmetry of the solution is evident from the two orthogonal diametral reflection planes (at $\theta_i = 0, \pi/2$) of the z-averaged cross-sectional contours. High- and low-speed streaks are clearly visible. In-plane velocity vectors show the location, on average, of the two pairs of counter-rotating vortices that are displayed in the three-dimensional view.
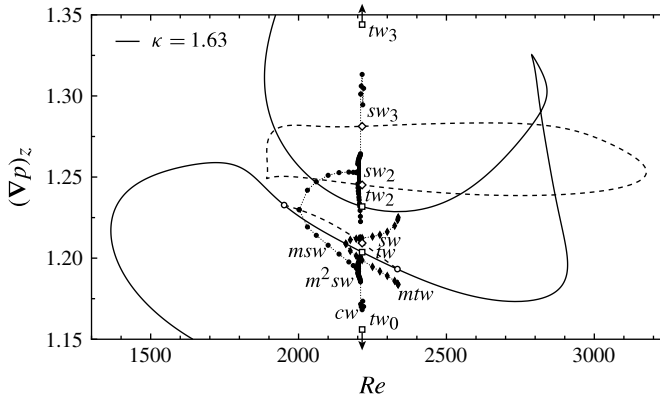
FIGURE 3. Mean axial pressure gradient ($(\nabla p)_z$) as a function of Re for $\kappa = 1.63$. Solid lines represent shift–reflect travelling waves; dashed lines are spiralling waves. Extrema of time-dependent travelling/spiralling solutions are marked as filled diamonds/circles, which denote Hopf bifurcations when placed on equilibria continuation curves. Open circles denote pitchfork bifurcations. Relative equilibria at $(\kappa, Re) = (1.63, 2215)$ are marked with open squares (tw_s, travelling waves from figure 2) and diamonds (sw_s, spiralling waves from figure 4). Modulated travelling, modulated spiralling, doubly modulated spiralling and chaotic waves are labelled mtw, msw, m^2sw and cw, respectively.

The behaviour of upper-branch waves for $\kappa = 1.63$ is shown in figure 3, where $(\nabla p)_z$ is plotted against Re. Upper-branch waves extend to moderate $Re \sim 2900$, then turn back in a contorted fashion towards lower values of the parameter, undergo a saddle-node bifurcation at about $Re \simeq 1885$ and finally progress towards much higher Re. As a result, four instances of the same solution coexist over a fairly wide Re-range. They are shown in figure 2 for $(\kappa, Re) = (1.63, 2215)$ and marked with open squares as tw_0, tw, tw_2 and tw_3 in figure 3. As already mentioned, the wave requiring the lowest driving axial pressure gradient (tw_0, on the lower branch, out of scale in figure 3 for clarity) lives on the laminar flow basin boundary. At the other end of the continuation curve, the waves exhibit driving pressure gradients in the region of turbulent flow values (tw_3, figure 2*d*, on the upper branch, also out of range in figure 3). The shift–reflect symmetry is clearly preserved but vorticity and axial velocity gradients in the vicinity of the wall are much more pronounced than for the lower-branch waves, as expected for turbulent solutions.

The waves tw and tw_2 we call lower- and upper-middle-branch waves, respectively, because of the relative values of their pressure gradients. As is clear from figure 2(*b*,*c*), they are also shift–reflect symmetric. The main properties of all members of this travelling wave family at $(\kappa, Re) = (1.63, 2215)$ are summarized in table 1.

3.2. *Spiralling waves*

A pair of symmetry-conjugate branches of spiralling waves bifurcates off the lower-middle-branch of shift–reflect waves (tw) in a symmetry-breaking pitchfork bifurcation (dashed line bounded by open circles in figure 3; see also figure 1). As a result of the loss of symmetry they start precessing in the azimuthal direction, but remain stationary in an appropriately spiralling frame of reference.

At the two pitchfork ends of the continuation curve, spiralling waves bifurcate with no rotation speed. As the asymmetry increases, rotation speed builds up reaching

	$(\nabla p)_z$	ν	c_z	$10^3 \times c_\theta$	$10^4 \times \varepsilon_{3D}$	$ev \in S$	$ev \in \bar{S}$
tw_0	1.1171	0.03228	1.5481	0.0	4.0964	$1r$	
tw	1.2037	0.03478	1.4600	0.0	7.5781	$1c$	$1r$
tw_2	1.2318	0.03559	1.4349	0.0	8.8704	$1r$	$1r$
tw_3	1.4738	0.04258	1.2891	0.0	19.280	$1c$	$1r + 2c$
sw	1.2093	0.03494	1.4583	± 0.9192	7.6261		$1c$
sw_2	1.2813	0.03702	1.4413	± 1.5964	8.4999		$1r + 1c$
sw_3	1.2451	0.03597	1.5015	± 1.9248	5.3584		$1c$

TABLE 1. Relative equilibria of the twofold azimuthally periodic subspace at $(\kappa, Re) = (1.63, 2215)$. The last two columns, $ev \in S$ and $ev \in \bar{S}$, count real (r) and complex pairs (c) of eigenmodes corresponding to the shift–reflect and shift–reflect-orthogonal subspaces, respectively. Tabulated travelling/spiralling waves are marked with open squares/diamonds in figure 3.
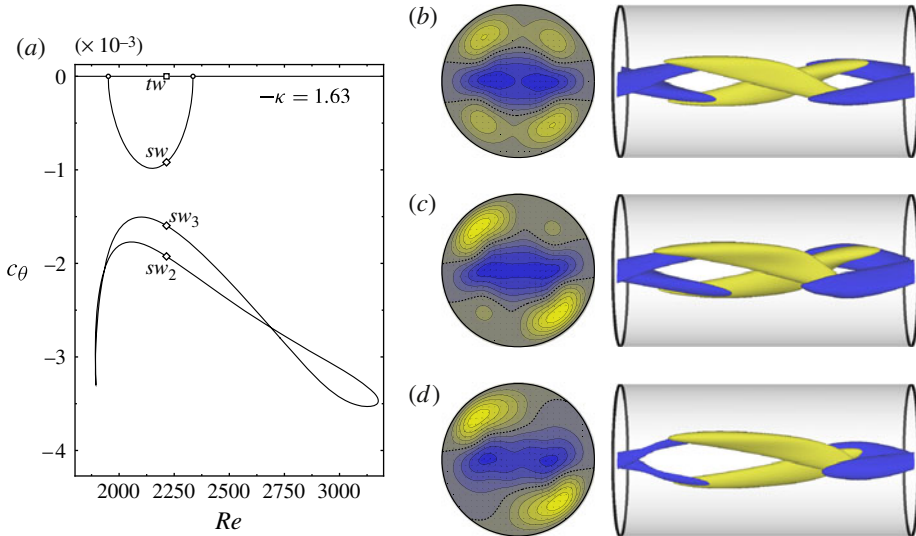
FIGURE 4. (Colour online) (*a*) Azimuthal drift speed (c_θ) of spiralling waves as a function of Re for $\kappa = 1.63$. Shift–reflect travelling waves collapse on the *x*-axis. Symbols and labels as for figure 3. (*b*) Lower-branch (*sw*), (*c*) middle-branch (sw_2) and (*d*) upper-branch (sw_3) spiralling waves at $(\kappa, Re) = (1.63, 2215)$. Contour levels and colour coding as for figure 2.

significant precessing rates, as shown in figure 4(*a*) (upper solid line labelled *sw*). The apparently disconnected branch of spiralling waves (dashed and solid closed loops of figures 3 and 4*a*, respectively), with higher rotation rates and extending to higher Re, reconnects with the other branch at lower κ. The details of the bifurcation whereby both branches merge are given in appendix A.

All the waves continued have negative rotation speed, but, obviously, their shift–reflected counterparts exhibit opposite azimuthal rotation. The azimuthal drift of the waves is much slower than their axial drift. As a matter of fact, the spiralling waves reported here travel a minimum of 700 wavelengths or 1350 diameters in the time they complete a full rotation.

As a result of the two disconnected branches at $(\kappa, Re) = (1.63, 2215)$, three different spiralling waves coexist: lower-, middle- and upper-branch waves, indicated by open diamonds and named sw, sw_2 and sw_3. They are shown in figure 4(*b–d*) and they all clearly break the shift–reflect symmetry. The spiralling wave most strongly related to tw is sw. They are close in parameter space (their continuation curves are connected) and they also look very much alike. Cross-sectional contours are strikingly similar, except that sw has slightly broken the shift–reflect symmetry. The other two spiralling waves, sw_2 and sw_3, have completely broken the symmetry and their rotation rates are much larger than for sw. The main properties of these spiralling waves at $(\kappa, Re) = (1.63, 2215)$ are summarized alongside those of travelling waves in table 1.

3.3. *Stability of travelling and spiralling waves*

The stability properties of travelling waves along the continuation surface is quite involved, with many eigenvalues changing sign repeatedly, and many states being related by the multiple folds present. A detailed study of these bifurcations is beyond the scope of the present analysis. Instead, we will concentrate on parameter regions where interesting dynamics occur and on stable waves that transition to more complex flows. Thus, we will set the wavenumber to $\kappa = 1.63$ and search for bifurcations of the lower-middle-branch travelling wave (tw) and the lower-branch spiralling wave (sw) by varying the Reynolds number. For an extended analysis with varying κ, see appendix A.

Figure 5 tracks the relevant (bifurcating) eigenvalues of tw and sw for $\kappa = 1.63$ and varying Re. A real eigenvalue of tw (black solid line) undergoes two zero-crossings (open circles) at $Re = 1951.1$ and $Re = 2335.2$, corresponding to the creation and destruction of the spiralling wave (sw) branch. Both pitchfork bifurcations are supercritical and the spiralling waves created have one less unstable direction than the travelling waves they originate from. In between the two pitchfork points, at about $Re = 2159.8$, a complex pair (black dashed line) crosses the imaginary axis at a Hopf point (black circle), and a branch of modulated travelling waves (mtw) appears. The initial modulational frequency of these waves is given by the imaginary part of the eigenvalue at the crossing. Here, $\omega = 0.02127 \,(4U/D)$, corresponding to a period $T = 2\pi/\omega = 295.5 D/(4U)$. Index theory dictates that, due to the travelling waves' stability properties just described, spiralling waves must be stable at the low-Re end and Hopf unstable at the high-Re end.

The complex pair duplicated on the spiralling branch (grey dashed line) takes the lead, in crossing the imaginary axis, from its travelling counterpart and undergoes a Hopf bifurcation (grey circle) somewhat earlier in Re, generating a branch of modulated spiralling waves (msw). These waves bifurcate at $Re = 2002.1$ with $\omega = 0.02214 \,(4U/D)$, corresponding to a period $T = 283.8 D/(4U)$, slightly shorter than for mtw. Both Hopf bifurcations are supercritical in the sense that the first Lyapunov coefficient is negative (Kuznetsov 1995) and the emerging modulated waves inherit the stability of the original waves.

The role of the rest of the travelling and spiralling waves is fairly irrelevant to the bifurcation cascade presented here. Nevertheless, a detailed analysis of the bifurcating eigenmodes reveals some of the connections among the waves, which persist once the chaotic set has been dismantled and may be of interest for further research on transition and turbulence in the subspace. For this reason, a short description of eigenmodes and connecting manifolds is reported in appendix B for completeness.
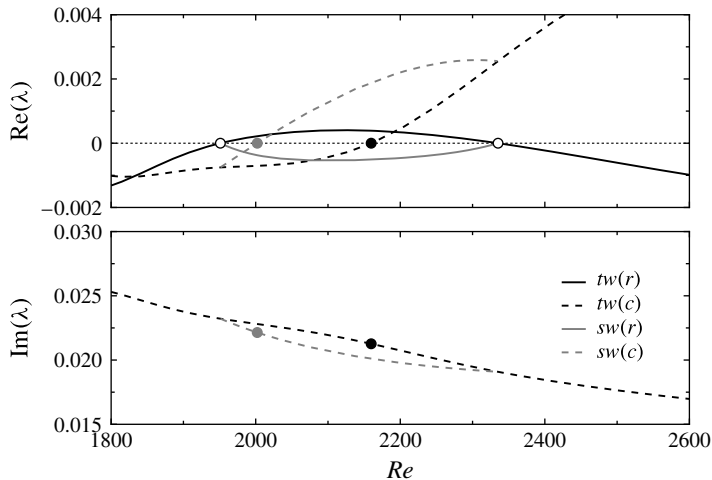
FIGURE 5. Real (solid) and complex (dashed) relevant eigenvalues of *tw* (black) and *sw* (grey) along their $\kappa = 1.63$-continuation curves. Open and filled circles correspond to pitchfork and Hopf bifurcation points, respectively.

4. Time-dependent solutions

The Hopf bifurcations prepare the stage for the appearance of time-dependent solutions. In this section, we analyse the modulated waves that result from the Hopf instabilities of travelling and spiralling waves described above.

4.1. *Modulated travelling waves*

In the symmetry-preserving Hopf bifurcation of the lower-middle travelling wave branch (*tw*) a shift–reflect symmetric time-periodic solution appears which is a modulated travelling wave (see figure 1), also referred to as a relative periodic orbit. As *Re* is increased, a complex pair of eigenvalues crosses into the unstable half of the complex plane as shown in figure 5 for $\kappa = 1.63$. In the κ-range of interest, the pitchfork bifurcation occurs before the Hopf bifurcation. As a consequence, modulated waves emerging from the Hopf instability, although supercritical, must be expected to inherit all previous instabilities. Accordingly, at $\kappa = 1.63$, emerging modulated travelling waves are pitchfork unstable at onset.

Fortunately, the Hopf instability lies precisely in the symmetry subspace that the pitchfork instability breaks, so that the latter can be suppressed by restricting time-evolution to the shift–reflect subspace. The fact that shift–reflect-restricted time-evolution unveils a stable branch of modulated travelling waves pointing towards increasing *Re* shows that the Hopf bifurcation is supercritical.

Thus, a branch of shift–reflect modulated travelling waves (*mtw*) has been unfolded at $\kappa = 1.63$ and represented in figure 3 (filled diamonds). The duplicity of symbols at each given *Re* denotes the maximum and minimum bounding values of the modulation. The shape of the continuation curve is suggestive of a turning point in a fold-of-cycles at about $Re \simeq 2337$, implying the existence of a saddle branch of cycles of larger amplitude. This was schematically shown in figure 1, and its consequences will be discussed below. Let us first focus on the nodal branch and analyse one of the solutions.
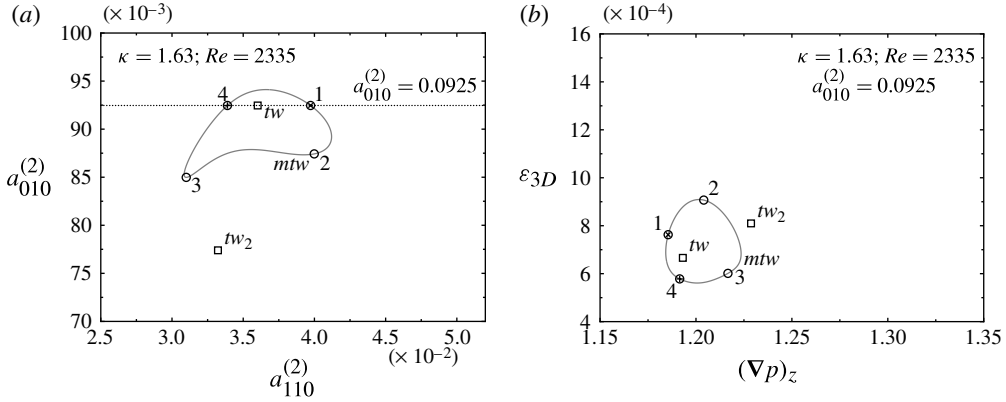
FIGURE 6. Phase map projections of a modulated travelling wave (*mtw*) at $(\kappa, Re) = (1.63, 2335)$. (*a*) $a_{010}^{(2)}$ versus $a_{110}^{(2)}$. (*b*) Three-dimensional energy (ε_{3D}) versus axial pressure gradient $((\nabla p)_z)$. Middle-branch travelling waves (*tw* and *tw*$_2$) are labelled and marked with open squares. Positive and negative crossings of a Poincaré section defined by $a_{010}^{(2)} = a_{010}^{(2)}(tw)$ are indicated by plus signs and crosses, respectively. Numbered circles correspond to snapshots in figure 8.

Figure 6 shows two alternative axial-drift-independent phase map projections of a modulated travelling wave solution at $(\kappa, Re) = (1.63, 2335)$. The solution describes a closed loop and can therefore be seen as a relative periodic orbit. The Hopf bifurcation adds a modulational frequency to the pure translational frequency. As a result, global quantities cease to be constant and oscillate with this frequency, while the representation of local quantities would have made the solution appear as quasiperiodic.

At $Re = 2335$, close to the presumed fold-of-cycles, the modulation has grown large around the travelling wave (*tw*) from which it originally bifurcated. To allow comparison with other solutions that will be discussed later, a drift-independent Poincaré section at $a_{010}^{(2)} = a_{010}^{(2)}(tw)$ has been defined. The trajectory pierces the Poincaré section twice, so it is convenient to differentiate between positive and negative crossings (plus signs and crosses, respectively, in figure 6).

The time-dependence is clarified by figure 7(*a*), where axial drift speed (c_z, black line) and mean axial pressure gradient $((\nabla p)_z$, grey line) time-series along a full period of the solution are represented. Comparing the time signals with the constant value for middle-branch travelling waves (*tw* and *tw*$_2$, horizontal dotted lines), it becomes clear that the modulated wave oscillates around *tw*, and seems to visit *tw*$_2$ once along every period, although figure 6 shows that it does not return too closely. Both signals oscillate $\pm 1\%$ around a mean value that has an offset when compared with *tw*. On average, the driving pressure gradient is slightly higher and the axial drift rate slower than for the travelling wave. This follows from the fact that we are no longer close to the bifurcation point and nonlinear effects have long since kicked in. The Fourier transform of the energy contained in non-axisymmetric streamwise dependent modes (ε_{3D}) is plotted in figure 7(*b*), with the time signal shown in the inset frame. The spectrum reveals that the solution has a strong mean component and a peak angular frequency at $\omega_0 = 0.0199\,(4U/D)$, corresponding to a period $T_0 = 2\pi/\omega_0 = 315.2 D/(4U)$. This period is extremely long when compared with the
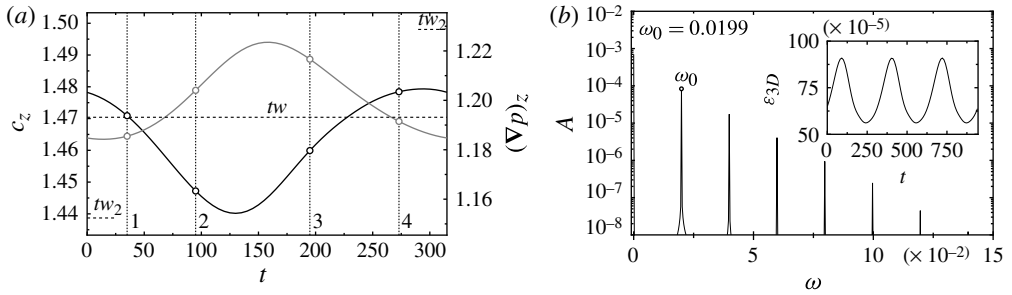
FIGURE 7. Modulated travelling wave (*mtw*) at $(\kappa, Re) = (1.63, 2335)$. (*a*) Axial drift speed (c_z, black line) and axial pressure gradient ($(\nabla p)_z$, grey line) time-series. Dotted horizontal lines indicate the values for *tw* and *tw*$_2$ while numbered vertical lines and open circles indicate snapshots in figure 8. (*b*) Fourier transform of the non-axisymmetric streamwise dependent modal energy contents (ε_{3D}). Part of the time signal is plotted in the inset.
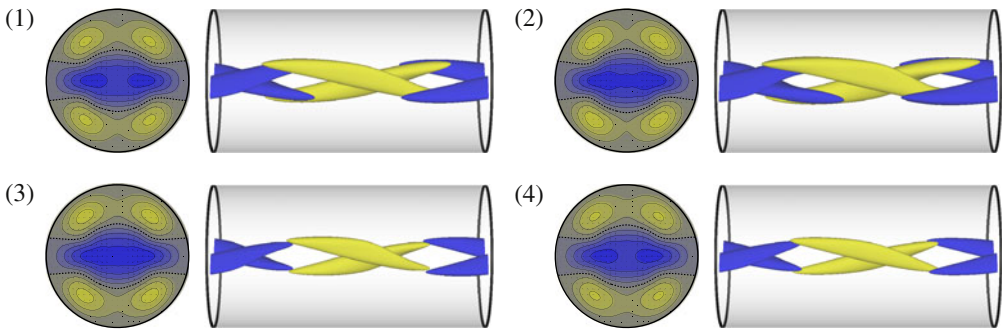

FIGURE 8. (Colour online) Modulated travelling wave at $(\kappa, Re) = (1.63, 2335)$. Contour levels and colour coding as for figure 2. To avoid drift due to streamwise advection, snapshots are taken in a co-moving frame moving with the instantaneous advection speed from figure 7(*a*). The snapshots are indicated by open circles in figures 6 and 7(*a*). (1) $t = 35$; (2) $t = 95$; (3) $t = 195$; (4) $t = 273$.

streamwise advection time scale, which is of order $2\pi/(\kappa c_z) \sim 3$. The signal is not strictly sinusoidal and some energy is spread among a number of harmonics of ω_0.

To better convey the modulational character of the instability, a few snapshots (conveniently marked in figures 6 and 7*a*) of the flow field along a cycle are represented in figure 8 (see online movie available at http://dx.doi.org/10.1017/jfm.2012.326). It is clear from the snapshots that the modulated wave indeed oscillates around *tw* (figure 2*b*) and that, as noted, preserves the shift–reflect symmetry. As expected from the mild oscillation of all time signals, the modulation is not very prominent and the snapshots all look fairly similar.

4.2. *Modulated spiralling waves*

The Hopf bifurcation on the branch of spiralling waves occurs at lower *Re* than on the branch of travelling waves (figure 5). Spiralling wave *sw* loses stability in a supercritical Hopf and a branch of stable modulated spiralling waves emerges (see
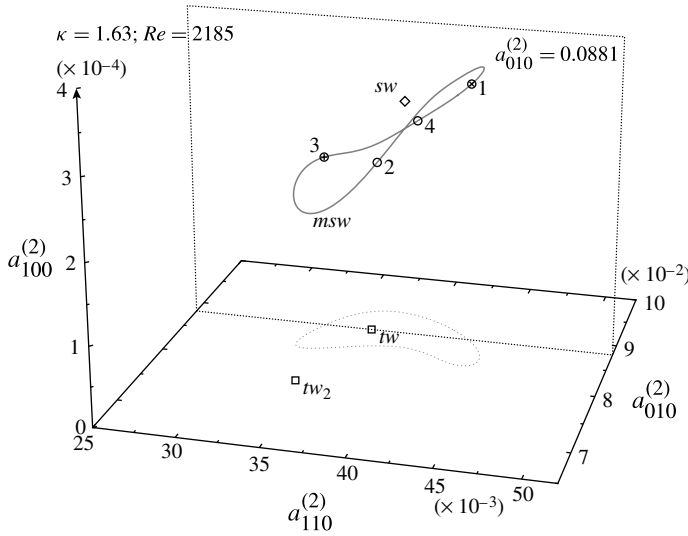
FIGURE 9. Three-dimensional phase map projection $(a^{(2)}_{010}, a^{(2)}_{110}, a^{(2)}_{100})$ of a modulated spiralling wave (*msw*) at $(\kappa, Re) = (1.63, 2185)$. Middle-branch travelling waves (*tw* and *tw*$_2$) are labelled and marked with open squares and the spiralling wave (*sw*) with an open diamond. Positive and negative crossings of a Poincaré section defined by $a^{(2)}_{010} = a^{(2)}_{010}(tw)$ are indicated by plus signs and crosses, respectively. Numbered circles correspond to snapshots in figure 12.

figure 1), pointing in the direction of increasing *Re*. The branch is plotted in figure 3 (filled circles, labelled *msw*) for $\kappa = 1.63$.

Figure 9 shows a three-dimensional phase map projection on the space defined by $(a^{(2)}_{010}, a^{(2)}_{110}, a^{(2)}_{100})$ of a modulated spiralling wave (*msw*) at $(\kappa, Re) = (1.63, 2185)$. The wave describes a closed loop in phase space surrounding the spiralling wave (*sw*) from which it bifurcated, and it does so at a finite amplitude of $a^{(2)}_{100}$, away from the shift–reflect subspace where this coefficient cancels exactly. The projection on the shift–reflect subspace (light grey dotted line on the $a^{(2)}_{100} = 0$ plane) is reminiscent of figure 6(*a*), even if they correspond to different *Re*, which suggests that both waves, *mtw* and *msw*, are related by a pitchfork of cycles at some other value of the parameters.

A couple of additional phase map projections are represented in figure 10. Figure 10(*a*) shows the projection of figure 9 on the $(a^{(2)}_{100}, a^{(2)}_{010})$ plane, while figure 10(*b*) represents the same trajectory in the $(\varepsilon_{3D}, (\nabla p)_z)$ plane. Comparison of the latter with figure 6(*b*) further supports the connection between *msw* and *mtw*.

In these phase map representations, since we are dealing with a modulated spiralling wave bifurcated from a spiralling wave, not only is the axial drift speed (c_z) masked, but also the azimuthal rotation rate (c_θ). Although only the modulational (Hopf) frequency is relevant to the dynamics, the two additional frequencies associated to the drifts have been recovered and plotted along a full period of *msw* in figure 11(*a*). They oscillate around the spiralling wave values with a certain offset due to nonlinear effects. Figure 11(*b*) shows the Fourier spectrum of the energy signal in the inset. As already observed for *mtw*, also *msw* has a slow modulation angular frequency of $\omega_0 = 0.0204\,(4U/D)$, corresponding to a period $T_0 = 307.8\,D/(4U)$. The fact that
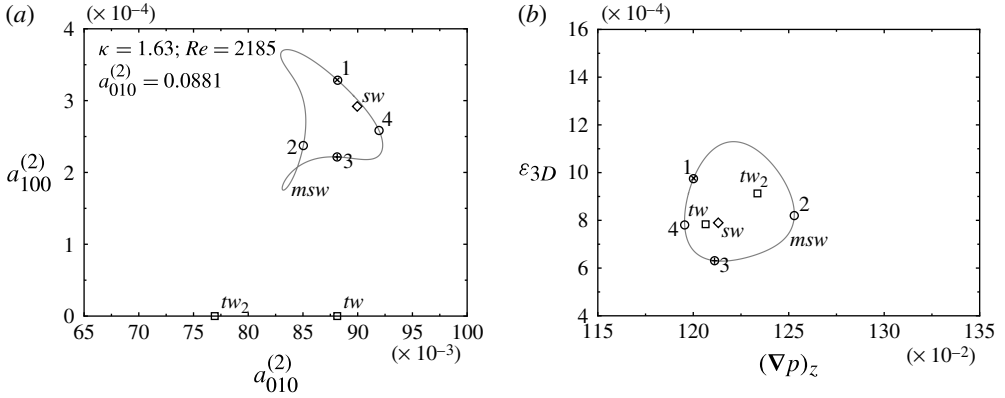
FIGURE 10. Phase map projections of a modulated spiralling wave (*msw*) at $(\kappa, Re) = (1.63, 2185)$. (*a*) $a_{100}^{(2)}$ versus $a_{010}^{(2)}$. (*b*) Three-dimensional energy (ε_{3D}) versus axial pressure gradient ($(\nabla p)_z$). Symbols and labels as for figure 9. The Poincaré section is defined by $a_{010}^{(2)} = a_{010}^{(2)}(tw)$. Numbered circles correspond to snapshots in figure 12.
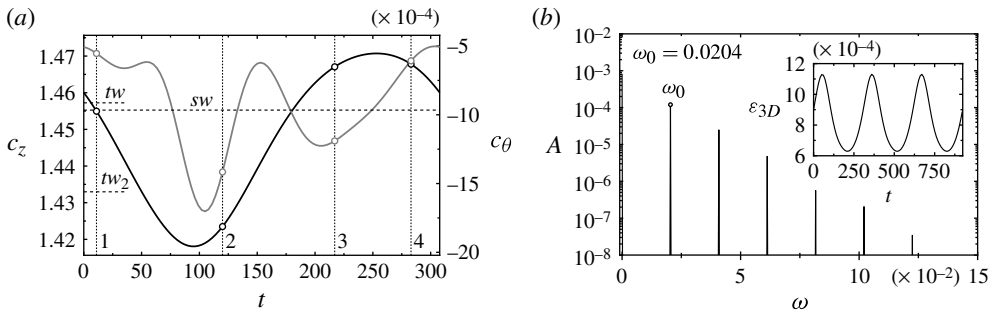

FIGURE 11. Modulated spiralling wave (*msw*) at $(\kappa, Re) = (1.63, 2185)$. (*a*) Axial ($c_z$, black line) and azimuthal (c_θ, grey line) drift speed time-series. Dotted horizontal lines indicate the values for *sw*, *tw* and *tw*$_2$ while numbered vertical lines and open circles indicate snapshots in figure 12. (*b*) Fourier transform of the non-axisymmetric streamwise dependent modal energy contents (ε_{3D}). Part of the time signal is plotted in the inset.

both periods are of the same order reinforces the suspicion that they are a consequence of the same mechanism.

Snapshots corresponding to the time instants indicated by circles in figures 9, 10 and 11(*a*) are plotted in figure 12 (see online movie). As was the case for *mtw* of figure 8, the modulational character of *msw* is very mild. Nevertheless, it clearly orbits around *sw* and the symmetry-breaking is fairly clear at all times.

4.3. *Doubly modulated spiralling waves*

For $\kappa = 1.63$, modulated spiralling waves undergo a supercritical Neimark–Sacker bifurcation (Hopf of cycles, as sketched in figure 1) that occurs away from strong resonances (Kuznetsov 1995). Bifurcated waves are relative quasiperiodic solutions involving two degenerate and two modulational frequencies, adding up to four frequencies. The two extrema (minimum and maximum) that were used to represent
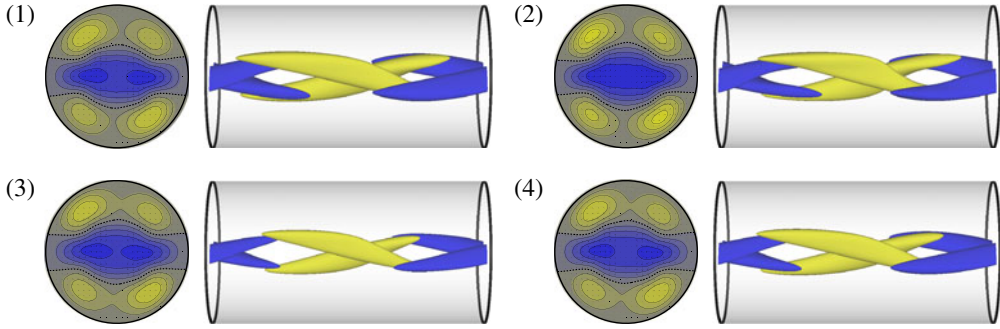
FIGURE 12. (Colour online) Modulated spiralling wave at $(\kappa, Re) = (1.63, 2185)$. Contour levels and colour coding as for figure 2. To avoid drift due to streamwise advection, snapshots are taken in a co-moving frame spiralling with the instantaneous advection speeds from figure 11(*a*). The snapshots are indicated by circles in figures 9, 10 and 11(*a*). (1) $t = 11$; (2) $t = 120$; (3) $t = 217$; (4) $t = 283$.
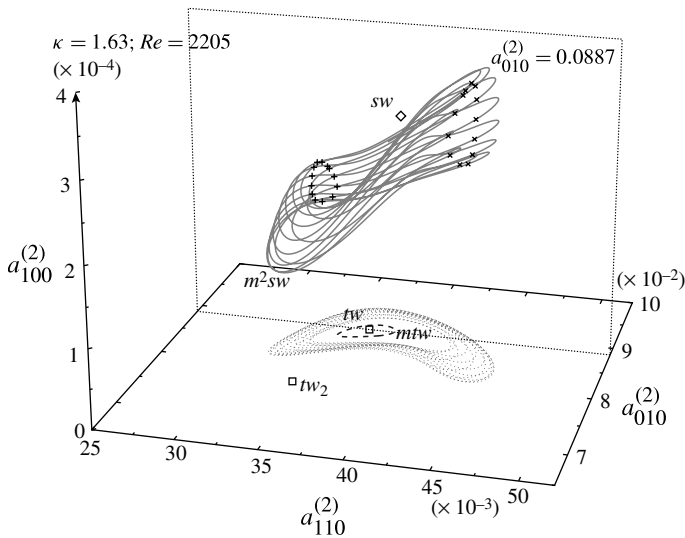

FIGURE 13. Three-dimensional phase map projection $(a_{010}^{(2)}, a_{110}^{(2)}, a_{100}^{(2)})$ of a doubly modulated spiralling wave (m^2sw) at $(\kappa, Re) = (1.63, 2205)$. Symbols and labels as for figure 9. The Poincaré section is defined by $a_{010}^{(2)} = a_{010}^{(2)}(tw)$.

modulated waves split in four to convey the existence of a modulation of the modulation (figure 3, filled circles, labelled m^2sw). The existence of doubly modulated waves at $\kappa = 1.63$ extends for a short range of less than 10 Re-units, which leaves enough room for them to evolve nonlinearly away from modulated waves so that they can be properly analysed.

Figure 13 shows a three-dimensional phase map projection on the space defined by $(a_{010}^{(2)}, a_{110}^{(2)}, a_{100}^{(2)})$ of a doubly modulated spiralling wave (m^2sw) at $(\kappa, Re) = (1.63, 2205)$. The modulated spiralling wave (msw) from which m^2sw bifurcates has gone unstable and is therefore inaccessible. Nevertheless, it can be safely presumed
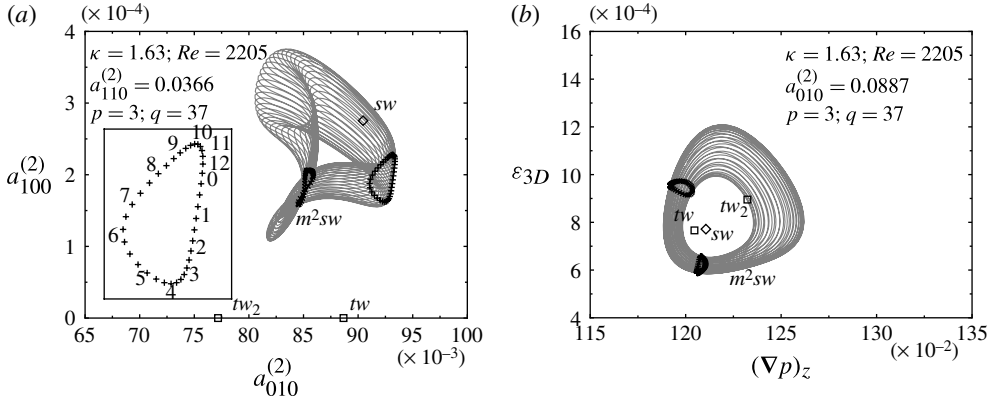
FIGURE 14. Phase map projections of a doubly modulated spiralling wave (m^2sw) at $(\kappa, Re) = (1.63, 2205)$. (a) $a^{(2)}_{100}$ versus $a^{(2)}_{010}$. The inset shows a Poincaré section defined by $a^{(2)}_{110} = a^{(2)}_{110}(tw)$. (b) Three-dimensional energy (ε_{3D}) versus axial pressure gradient (($\nabla p)_z$). The Poincaré section is defined by $a^{(2)}_{010} = a^{(2)}_{010}(tw)$. Symbols and labels as for figure 9.

that it looks similar to *msw* as shown for $Re = 2185$ in figure 12 and that it must be contained within the region of phase space delimited by the invariant torus on which m^2sw runs. Looking at the Poincaré section, it is easy to identify the drift undergone by the wave after every flight. The drift goes in a rough circle, appearing as an invariant cycle on the Poincaré map.

Doubly modulated waves will generally be densely filling on the torus (quasiperiodic), since no resonant conditions are enforced by any of the symmetries of the problem and the new frequency does not necessarily need to be commensurate with the previously existing modulation frequency inherited from the modulated wave. However, as the parameter is varied, Arnold tongues might be crossed and phase locking occur, producing parameter windows where periodic orbits exist. The torus persists under small parameter variations but the orbit structure will be dependent on whether the rotation number of the map defined by Poincaré reduction is rational or irrational. As a matter of fact, the wave shown in figure 13 exhibits a rational proportion between the two frequencies, as can be seen in figure 14. The orbit structure and the Poincaré sections clearly show that the wave is a (3, 37)-cycle: the cycle makes 37 revolutions along the modulated wave trajectory (short modulation period) and 3 around the invariant curve on the Poincaré map (long modulation period) before closing. The 37th iterate of the Poincaré map is therefore a fixed point. The existence of a stable (3, 37)-cycle implies that an unstable (3, 37)-cycle must also exist (Kuznetsov 1995). This is the only phase locking identified in this study, meaning that all other doubly modulated waves found are dense or, at least, of extremely long period.

The Neimark–Sacker modulational frequency is much higher than the inherited Hopf frequency. Drift speed time-series along a full cycle around the Poincaré section for the wave at $(\kappa, Re) = (1.63, 2205)$ are shown in figure 15(a). The signal is of about the same frequency as that in figure 11(a), but now it is slightly modulated with a much longer period. The spectrum of the energy signal shown in figure 15(b) features the same peaks, corresponding to the fast modulation $\omega_0 = 0.0203$, as that of the modulated wave (figure 11b), except that additional peaks at multiples of the slow
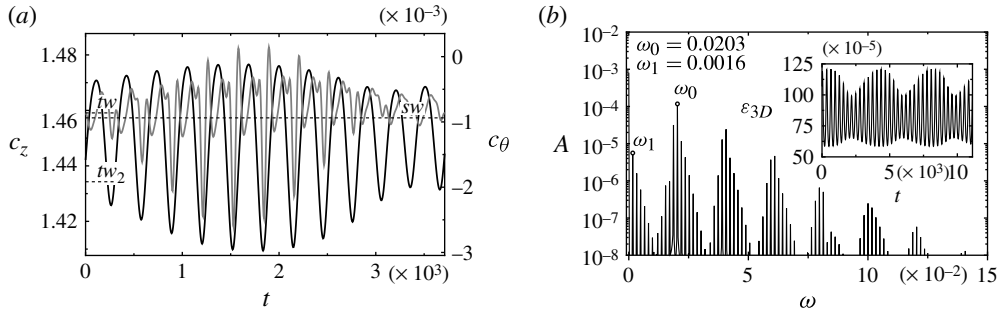
FIGURE 15. Doubly modulated spiralling wave (m^2sw) at $(\kappa, Re) = (1.63, 2205)$. (a) Axial ($c_z$, black line) and azimuthal (c_θ, grey line) drift speed time-series. Dotted horizontal lines indicate the values for *sw*, *tw* and *tw*$_2$. (b) Fourier transform of the non-axisymmetric streamwise dependent modal energy contents (ε_{3D}). Part of the time signal is plotted in the inset.

frequency $\omega_1 = 0.001649$ appear in the scene. The spectrum is still discrete, as should be expected from a quasiperiodic signal, but now two frequencies are identifiable. In this case, due to phase locking, the ratio of frequencies is rational and coincides precisely with the rotation number ($\rho = \omega_1/\omega_0 = p/q = 3/37$).

The slow period is very long ($T_1 = 2\pi/\omega_1 \simeq 3810.3D/(4U)$), which makes it difficult to select just a few snapshots that are representative of the time-dependence of the wave (see online movie). Nevertheless, the modulation along the short period has already been exemplified for a modulated spiralling wave in figure 12 and should be fairly similar for a bifurcated doubly modulated wave. We have set the focus on the slow modulation effect by analysing the drift experienced by the wave every time the Poincaré section is pierced. The solution, which originally bifurcated at zero amplitude with respect to the modulated spiralling wave, has barely left the linear regime. Consequently, the modulation is extremely mild and only a close inspection reveals that there is any modulation at all. The effect becomes more prominent for slightly higher *Re* and will be discussed later.

Increasing *Re* at $\kappa = 1.63$ results in a significant swell of the invariant torus and an ulterior catastrophic transition into a chaotic attractor.

4.4. *Mildly chaotic spiralling waves*

Doubly modulated spiralling waves cease to exist abruptly and the new dynamics are organized along pseudoperiodic trajectories. These solutions largely preserve some of the features of the original torus at some stages but depart wildly at some other stages. Reattachment to the remnants of the torus never occurs at the same point, introducing a mild degree of chaoticity.

A full pseudoperiod of a time-evolving chaotic spiralling wave (*cw*) at $(\kappa, Re) = (1.63, 2215)$ is represented in figure 16. For a while, the orbit runs on the remnants of the invariant torus that existed at lower *Re* (figure 13). As it goes around, though, the flow is unable to close as before, and the trajectory is thrown away and gets hooked in a seemingly periodic motion as if it was captured by the stable manifold of some periodic orbit. All this happens at very low $a_{100}^{(2)}$, which is indicative of a close approach to the shift–reflect subspace. After some turns, the trajectory departs again with a violent thrust and then reconnects back onto what seems to be the unstable
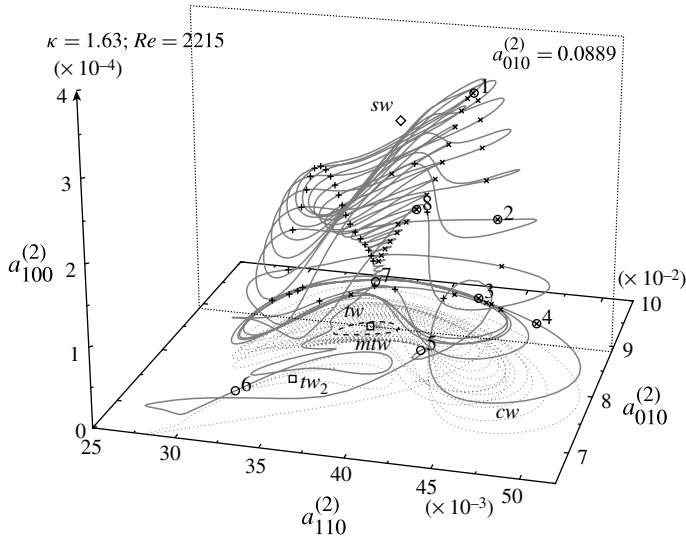
FIGURE 16. Three-dimensional phase map projection $(a_{010}^{(2)}, a_{110}^{(2)}, a_{100}^{(2)})$ of a chaotic spiralling wave (cw) at $(\kappa, Re) = (1.63, 2215)$ along a full pseudoperiod. Symbols and labels as for figure 9. A coexisting modulated travelling wave $(mtw$, black dashed line) is also represented. The Poincaré section is defined by $a_{010}^{(2)} = a_{010}^{(2)}(tw)$. Numbered circles correspond to snapshots in figure 19.
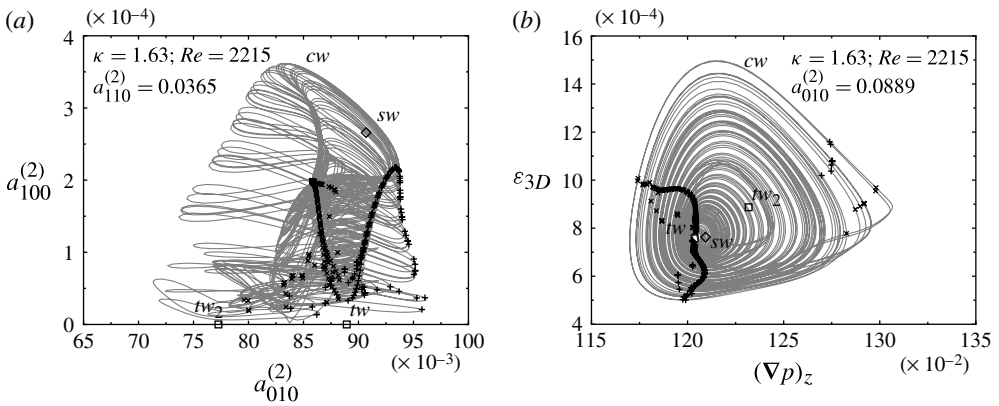

FIGURE 17. Phase map projections of a chaotic spiralling wave (cw) at $(\kappa, Re) = (1.63, 2215)$ along several pseudoperiods. (a) $a_{100}^{(2)}$ versus $a_{010}^{(2)}$. Marks indicate crossings of a Poincaré section defined by $a_{110}^{(2)} = a_{110}^{(2)}(tw)$. (b) Three-dimensional energy (ε_{3D}) versus axial pressure gradient $((\nabla p)_z)$. The Poincaré section is defined by $a_{010}^{(2)} = a_{010}^{(2)}(tw)$. Symbols and marks as for figure 9.

manifold of tw. Finally, following this manifold, the trajectory makes its trip back onto the torus-dominated region and the process starts anew.

Several pseudoperiods of the wave are represented in a couple of phase map projections (figure 17) to illustrate its mildly chaotic character. The Poincaré map in figure 17(a) tends to be dense and deterministic at the upper tip, where the solution
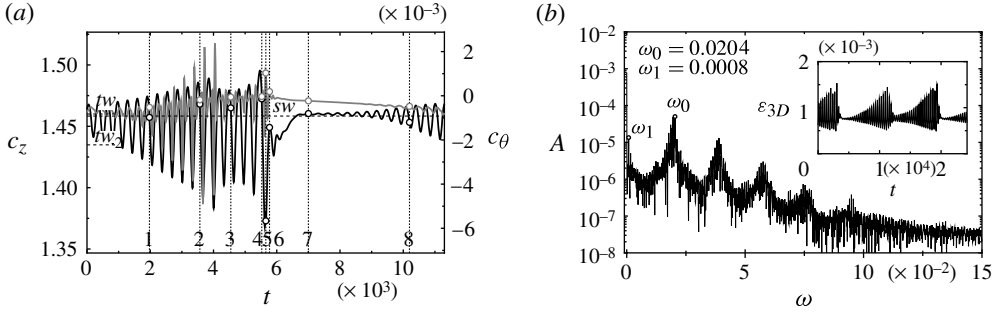
FIGURE 18. Chaotic spiralling wave (*cw*) at $(\kappa, Re) = (1.63, 2215)$. (*a*) Axial ($c_z$, black line) and azimuthal (c_θ, grey line) drift speed time-series. Dotted horizontal lines indicate the values for *sw*, *tw* and *tw*$_2$ while numbered vertical lines and open circles indicate snapshots in figure 19. (*b*) Fourier transform of the non-axisymmetric streamwise dependent modal energy contents (ε_{3D}). Part of the time signal is plotted in the inset.

runs on the torus (to be compared with figure 14*a*). Meanwhile, the lower side features a chaotic cloud of random crossings. Furthermore, the return funnel that gets the trajectory back on the torus exhibits a variable width that can get as narrow as in figure 16. The ε_{3D} versus $(\nabla p)_z$ phase map also gives a clear view on the fate of the torus. While at $Re = 2205$ (figure 14*b*) the doughnut shape with closed *mtw*-centred orbits on the Poincaré sections was clearly identifiable, at $Re = 2215$ (figure 17*b*), the hole has been disrupted and long excursions to high three-dimensional energy values and large axial pressure gradients occur.

Time signals preserve the fast frequency associated to the old Hopf instability, while the slow frequency resulting from the Neimark–Sacker instability is substituted by a longer period modulation that is no longer constant. Drift speed time-series for a pseudoperiod of the chaotic wave at $(\kappa, Re) = (1.63, 2215)$ are drawn in figure 18(*a*). Both signals undergo a steady amplitude growth before becoming somewhat chaotic. Drift speed modulations get fairly large just before the chaotic transient, with the azimuthal drift speed (c_θ) even changing sign, which means that at some intervals the wave becomes retrograde. Towards the end of the chaotic transient, the azimuthal drift speed vanishes as the wave approaches the shift–reflect subspace and, shortly after, the axial drift speed (c_z) evolves towards lower-middle-branch travelling wave values (*tw*). From there on, the wave evolves as if it was following the combined pitchfork-Hopf-unstable manifold of *tw* and the process restarts. It is remarkable how, despite the close visit to the shift–reflect subspace, and even if the azimuthal speed changes sign, the wave always makes its way back to the same side of phase space. There are no reversals, contrary to what happens for the Lorenz attractor (Strogatz 1994), and the shift–reflect-conjugate side of phase space is never visited. Therefore, a shift–reflect symmetric chaotic attractor spiralling with opposite rotation rate exists and the two attractors do not interact.

The inset of figure 18(*b*) illustrates the variable nature of the long modulational period. The spectral energy density of the signal reflects this variability. There still are clear peaks at the high frequency $\omega_0 = 0.0204 \, (4U/D)$ and its harmonics, largely preserved from modulated and doubly modulated spiralling waves. The long period modulation, though, is no longer represented by a discrete peak, but by a certain dispersal around $\omega_1 \simeq 0.0008 \, (4U/D)$. The pseudoperiod is much longer than for
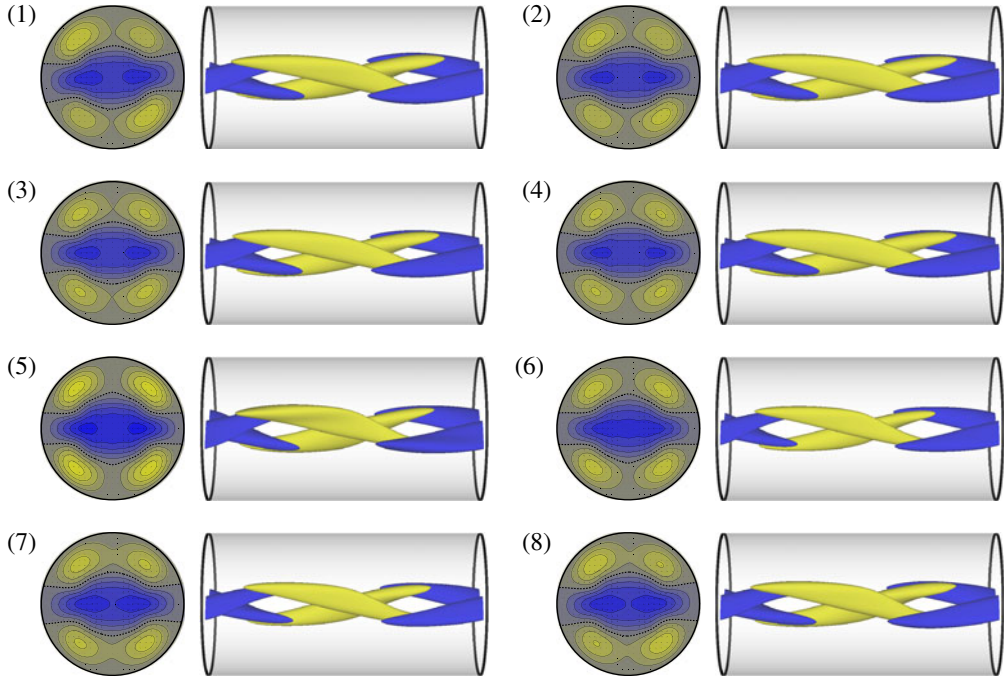
FIGURE 19. (Colour online) Chaotic spiralling wave at $(\kappa, Re) = (1.63, 2215)$. Contour levels and colour coding as for figure 2. To avoid drift due to streamwise advection, snapshots are taken in a co-moving frame spiralling with the instantaneous advection speeds from figure 18(a). The snapshots are indicated by circles in figures 16 and 18(a). (1) $t = 1974$; (2) $t = 3569$; (3) $t = 4547$; (4) $t = 5526$; (5) $t = 5654$; (6) $t = 5771$; (7) $t = 7000$; (8) $t = 10\,196$.

doubly modulated waves due to the fact that the wave spends large amounts of time in a region of phase space not visited by m^2sw. The effect of the dispersal is that the wave ceases to be quasiperiodic and the spectrum becomes continuous.

To illustrate the time-dependence of the flow field, several snapshots of the chaotic spiralling wave along a pseudoperiod have been gathered in figure 19. To reduce the number of snapshots to a minimum, but still illustrate the fate of m^2sw, flow fields have been represented either on the Poincaré section defined in figure 17 (snapshots 1–4 and 8) or along the violent escape in the vicinity of the shift–reflect subspace (snapshots 5 and 6).

Snapshots (1), (2) and (8) of figure 19 correspond to time instants at which the trajectory runs on the torus. As such, they illustrate the evolution of m^2sw as it grows. Snapshots (3) and (4), notwithstanding the fact that they correspond to Poincaré crossings, exemplify new dynamics. They are in a region of phase space away from where the torus existed and very close to the shift–reflect subspace, as is apparent from the clearly identifiable quasi-symmetry planes of the cross-sections. Snapshot (3) belongs in the region where cw seems to get hooked on a periodic orbit, while snapshot (4), taken at the time the violent excursion starts, seems to confirm it, as it bears a great similarity to (3). The axial pressure gradient peak in figure 17(b) is represented by snapshot (5), where the streaks are clearly very strong and the shift–reflect symmetry fairly clear. Snapshot (6) shows the closest
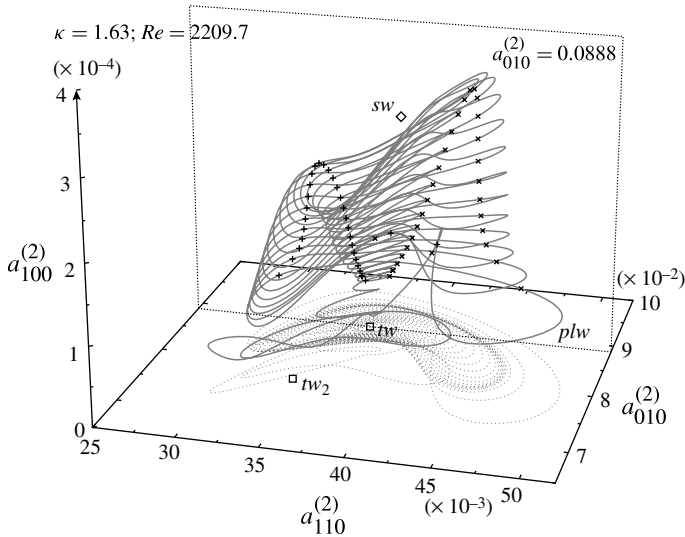
FIGURE 20. Three-dimensional phase map projection $(a_{010}^{(2)}, a_{110}^{(2)}, a_{100}^{(2)})$ of a phase-locked spiralling wave (*plw*) at $(\kappa, Re) = (1.63, 2209.7)$ along a full period. Symbols and marks as for figure 9. The Poincaré section is defined by $a_{010}^{(2)} = a_{010}^{(2)}(tw)$.

visit to the shift–reflect subspace and is, at the same time, a disputably close visit to tw_2 (figure 2c) as indicated by both cross-sectional axial velocity contours and axial vorticity isosurfaces. Snapshots (4–6) occur in a small fraction of the full trajectory, which ultimately justifies the description of the escape as violent. The shift–reflect symmetry starts being disrupted again in snapshot (7) and the wave evolves slowly as if departing away from *tw* along its unstable pitchfork-Hopf manifold. The flow field in (7) is clearly halfway between *tw* (figure 2b) and *sw* (figure 4a). At (8) the symmetry has been completely broken and the flow field reattaches to the remnants of the invariant torus.

4.5. *Phase-locked wave*

As in many systems (see e.g. the logistic map in Strogatz 1994) where a chaotic attractor develops, there exist parameter intervals where the solution locks onto a stable periodic orbit. These are called periodic windows, and the chaotic set described above is no exception.

At $Re = 2209.7$, very slightly above torus breakdown and creation of the chaotic set, and for a tiny interval, the flow becomes periodic. The periodic trajectory, which looks very similar to the pseudoperiodic trajectory at $Re = 2215$, is represented in figure 20.

Drift speeds are plotted in figure 21(a) for comparison with *cw*. Chaos disappears but the invariant torus is not re-established and the shift–reflect escape is preserved. The slowly evolving interval that we identified as an approach to the unstable manifold of *tw* is no longer as clear, and the return funnel is wide from the beginning, so that amplitude modulation is present all along. Despite the close resemblance of all time signals to some of the pseudoperiods at $Re = 2215$, time stamps are now strictly periodic and the Fourier transform of three-dimensional energy time-series is again discrete, as was the case at $Re = 2205$. The fast frequency $\omega_0 = 0.0204\,(4U/D)$ is clearly identifiable with the Hopf instability, while the slow
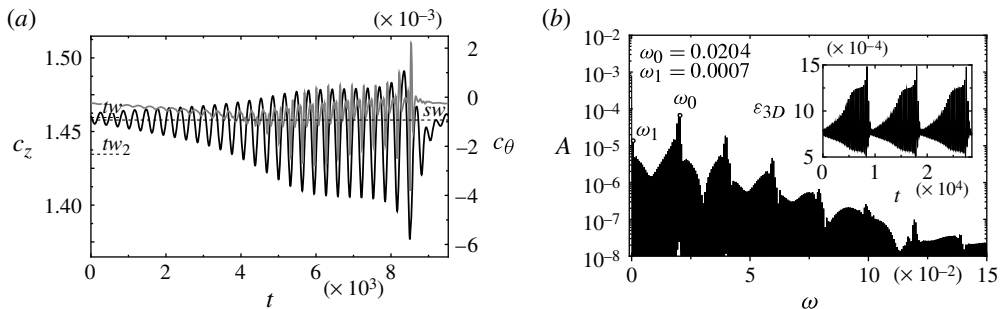
FIGURE 21. Phase-locked spiralling wave (*plw*) at $(\kappa, Re) = (1.63, 2209.7)$. (*a*) Axial ($c_z$, black line) and azimuthal (c_θ, grey line) drift speed time-series. Dotted horizontal lines indicate the values for *sw*, *tw* and *tw*$_2$. (*b*) Fourier transform of the non-axisymmetric streamwise dependent modal energy contents (ε_{3D}). Part of the time signal is plotted in the inset.

frequency $\omega_1 = 0.0006596 \,(4U/D)$ is inherited from *cw* but now takes a sharp value and fits exactly an integer number of times in ω_0.

We do not provide snapshots of the flow structures at selected times along a period because of the close resemblance they bear to those shown for $Re = 2215$ in figure 19.

4.6. *Turbulent transients*

At somewhat larger *Re* the chaotic set ceases to be an attractor and cannot hold trajectories indefinitely. Figure 22 exemplifies two departures from the chaotic set at $\kappa = 1.63$ and $Re = 2235$ and 2240. Logarithmic scale has been used for the vertical axis to aid visualization. The dense structure in the middle of the figure is the remains of the chaotic attractor, which preserves the same structure as for lower *Re*, except that it is no longer an attractor. For both Reynolds numbers shown, the solution departs in pretty much the same direction towards the region in phase space where the strongly spiralling waves *sw*$_2$ and *sw*$_3$ are. At $Re = 2235$ (figure 22*a*), the trajectory does not reach the waves and relaminarization soon follows. Instead, at $Re = 2240$ (figure 22*b*), the flow reaches the location where spiralling waves live and is kicked towards turbulence. The solution stays turbulent for around $1000D/(4U)$ and finally relaminarizes, oddly enough, along a path that seems close to that followed at $Re = 2235$.

Full understanding of the actual nature of the twofold azimuthally symmetric turbulent saddle is beyond the scope of this study and the issue will not be pursued further. It is nevertheless pertinent to stress that turbulence does occur within the azimuthal subspace and even when computations are further restricted to preserve the shift–reflect symmetry.

5. Formation and destruction of the chaotic attractor

Most of the transitions between states reported here are of a local nature and belong to simple bifurcation scenarios, once the drifts due to axial and azimuthal degeneracy are removed. This is not the case for the transition from doubly modulated waves to mildly chaotic waves. There are several known paths whereby deterministic solutions revolving around an invariant torus become chaotic when the torus disappears. Some of them have been described in the context of turbulent
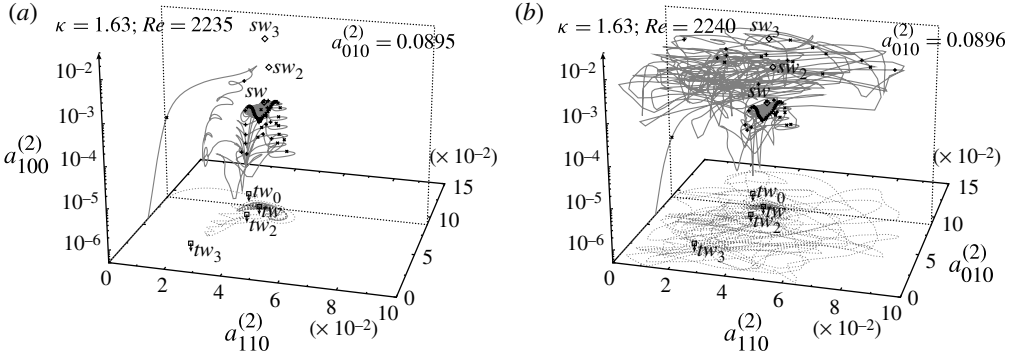
FIGURE 22. Three-dimensional phase map projection $(a_{010}^{(2)}, a_{110}^{(2)}, a_{100}^{(2)})$ of two escapes from the chaotic set. (a) $(\kappa, Re) = (1.63, 2235)$. (b) $(\kappa, Re) = (1.63, 2240)$. Travelling waves ($tw_0$, tw, tw_2 and tw_3) are labelled and marked with open squares and spiralling waves (sw, sw_2 and sw_3) with open diamonds. Positive and negative crossings of a Poincaré section defined by $a_{010}^{(2)} = a_{010}^{(2)}(tw)$ are indicated by plus signs and crosses, respectively.

transition. Landau (1944) suggested quasiperiodic motion resulting from an infinite cascade of bifurcating incommensurable frequencies that ultimately lead to turbulence. Ruelle & Takens (1971) and Newhouse, Ruelle & Takens (1978) modified the scenario to include dissipative systems, such as viscous fluids, that do not, in general, have quasiperiodic motions. Their route to chaos involved successive bifurcations from a stable equilibrium into a stable limit cycle followed by transition to a stable 2-torus and then to chaos. The scenario, though, does not give a full description of all possible bifurcation scenarios leading to the destruction of a 2-torus and does not provide conditions under which chaos may or may not follow. Some scenarios have been analysed by generalizing Floquet theory in systems without symmetry (Chenciner & Iooss 1979) and some theorems on torus breakdown have been formulated (Anischenko, Safonova & Chua 1993). These theorems, known by the name Afraimovich–Shilnikov theorems, suggest three distinct scenarios: (i) breakdown due to some ordinary bifurcation of phase-locked limit cycles such as period doubling (flip) or Neimark–Sacker type; (ii) sudden transition to chaos due to the appearance of a homoclinic connection; (iii) breakdown following from a gradual loss of smoothness. We will argue that along our one-dimensional path we follow scenario (ii).

Very valuable information can be retrieved from the frequency of quasiperiodic solutions as they approach the bifurcation point. As shown in figure 23(a), the fast angular frequency (ω_0) evolves smoothly through the Neimark–Sacker bifurcation from modulated to doubly modulated waves – so much so that the bifurcation point for $\kappa = 1.63$ (black solid line) at $Re \sim 2199$ is not discernible, and doubly modulated waves inherit this Hopf frequency directly from modulated waves. As quasiperiodic motion evolves, the frequency grows slightly but remains bounded, experiences a small bump, and then stabilizes at a fairly constant lower value (on average) for chaotic waves after the global bifurcation has taken place. In contrast, the slow frequency (ω_1) experiences substantial variation across the bifurcation, as is evident from figure 23(b). Since the two frequencies associated to degenerate drifts (mean values of c_z and c_θ) and ω_0 evolve smoothly across the bifurcation, while the period $T_1 = 2\pi/\omega_1$ becomes unbounded, we will represent the 4-torus as a limit cycle and relative limit cycles as
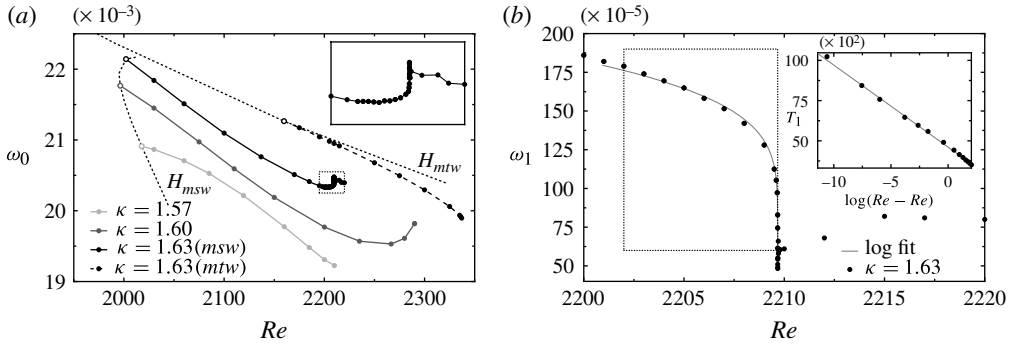
FIGURE 23. (*a*) Fast angular frequency (ω_0) of all time-dependent solutions as a function of *Re* and κ. Solid lines for spiralling waves and dashed lines for travelling waves (line shading for varying κ as indicated in the legend). Hopf bifurcation curves are indicated by dotted lines and labelled (H_{mtw} and H_{msw}). The inset shows a close-up of the small dotted square. (*b*) Slow frequency (ω_1) of doubly modulated waves at $\kappa = 1.63$. The inset shows a close-up of the dotted-square-region with a coordinate transformation ($T_1 = 2\pi/\omega_1$ versus $\log(Re_c - Re)$).

equilibria. We can do this because constant and nearly constant frequencies do not play a role in the dynamics near bifurcation points.

Infinite-period bifurcations are commonly associated with homoclinic or heteroclinic behaviour. The two most typical cases are the saddle-node and the saddle-loop homoclinic bifurcations, depending on whether the bifurcating orbit becomes homoclinic to a non-hyperbolic or to an hyperbolic equilibrium, respectively (Strogatz 1994; Kuznetsov 1995). One of the measurable properties that allows discrimination between the two is the way in which the period diverges. When a saddle-node develops on a limit cycle, the period diverges according to

$$T_1 = \frac{2\pi}{\omega_1} \sim \frac{C}{\sqrt{Re_c - Re}} + D, \tag{5.1}$$

where Re_c is the critical *Re*, and *C* and *D* are fitting parameters. In contrast, when a cycle grows to collide with a hyperbolic saddle and then disappear in a saddle-loop bifurcation, the period diverges logarithmically, as (Gaspard 1990)

$$T_1 = \frac{2\pi}{\omega_1} \sim -\lambda^{-1} \log(Re_c - Re) + D, \tag{5.2}$$

where the factor λ is the eigenvalue of the unstable direction of the hyperbolic fixed point and log represents the natural logarithm.

The behaviour of the period near a saddle-loop bifurcation may be extended to more complex scenarios such as Shilnikov bifurcations in *n*-dimensional dynamical systems or even torus collision with hyperbolic limit cycles (Marques, Lopez & Shen 2001), while the saddle-node homoclinic trend is also observed in the case of orbits homoclinic to non-hyperbolic equilibria or to other non-hyperbolic cycles, for example a blue sky catastrophe (Meca *et al.* 2004), but also in the case when the invariant set forms a torus.

The frequency range of the doubly modulated waves is in very good agreement with a logarithmic fit (5.2) (grey solid line in figure 23*b* – see the inset). As
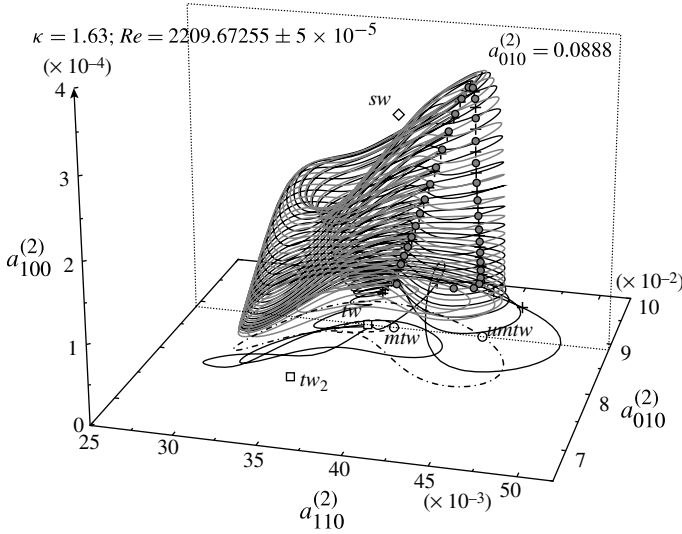
FIGURE 24. Three-dimensional phase map projection $(a_{010}^{(2)}, a_{110}^{(2)}, a_{100}^{(2)})$ just before (grey, circles for Poincaré crossings) and after (black, plus signs) transition. Symbols and labels as for figure 9. The shift–reflect stable (*mtw*) and unstable (*umtw*) modulated waves are indicated by dashed and dash-dotted lines, respectively.

a result of the fit, an estimated value of $Re_c = 2209.67253$ is obtained for the critical bifurcation point and $\lambda = 1.959 \times 10^{-3}\,(4U/D)$. This suggests that the torus might become homoclinic to a hyperbolic saddle cycle with an unstable multiplier of $\mu = e^{\lambda T_0} \simeq 1.8253$ (where $T_0 = 307.2D/(4U)$ is the fast period of trajectories on the torus, which should coincide, in the limit, with the period of the saddle cycle) as the bifurcation is approached.

The evolution of the frequency suggests an approach to a homoclinic or, as we will see, a heteroclinic-cyclic connection involving hyperbolic orbits. To elucidate with which solution or solutions the torus collides, we have analysed trajectories corresponding to refined approaches to the transition point from either side of the bifurcation. Figure 24 shows a three-dimensional phase map representation of the stable solution just before (doubly modulated wave, grey solid line) and after (mildly chaotic wave, black solid line) transition. For a large fraction of the time, both solutions run together, as is clear from the upper part of the plot. However, as the solutions spiral down the outer side of the torus and approach the shift–reflect subspace, the doubly modulated wave closes on the torus from below, while the chaotic wave is kicked away and moves in a disordered way in the vicinity of the shift–reflect subspace for a while before joining the torus back at the inner side to spiral up. The divergence of the trajectories is further in evidence when comparing the crossings on the Poincaré section (open circles for the quasiperiodic wave, plus signs for the chaotic wave). The Poincaré map associated to the doubly modulated wave describes a triangle-shaped cycle, while the chaotic wave only preserves the upper part of the triangle and breaks down at the lower side. The solutions, as shown in the figure, only revolve once around the torus, but they fill the trajectories on the Poincaré map densely when followed for sufficiently long times.

Figure 25 shows these solutions on the Poincaré section, together with an array of solutions at a varying distance from either side of the bifurcation point. As transition is
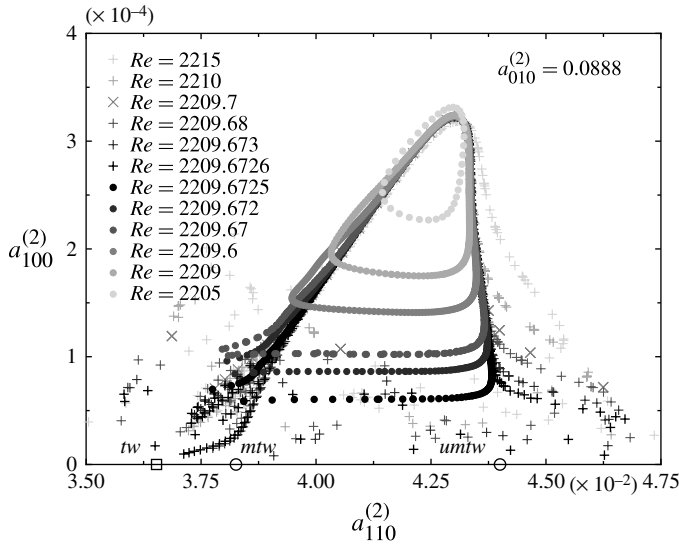
FIGURE 25. Poincaré section showing solutions before (filled circles) and after (plus signs and crosses for phase-locked wave) transition. The travelling wave (*tw*) is labelled and marked with an open square. The shift–reflect stable (*mtw*) and unstable (*umtw*) modulated waves are indicated by open circles.

approached from $Re < Re_c$ (filled circles getting darker), the cycle gets more and more triangle-shaped, starting from the phase-locked pseudo-circular shape at $Re = 2205$. The cycles run clockwise. The upper corner remains fixed, while the lower side gets aligned with the shift–reflect subspace, represented by the horizontal axis, and approaches it in a blow-up fashion (note that solutions are not Re-equispaced). For each quasiperiodic wave, a fairly equidistant chaotic wave at the other side of the transition point is represented (plus signs for the chaotic waves, crosses for the phase-locked wave at $Re = 2209.7$). The right side of the chaotic wave closes on the right side of the quasiperiodic wave like a zipper as bifurcation is approached. After departing from the right vertex of the triangle, chaos follows and reattachment to the left side of the torus is less regular.

The trend followed by the right vertex of the triangle suggests that a shift–reflect saddle cycle (a fixed point of the Poincaré map) might be approached. The chaotic dynamics clouds the behaviour near the left vertex somewhat, but we suspect that it approaches the modulated travelling wave (*mtw*). This modulated travelling wave, a stable node in its shift–reflect subspace, was presumed to undergo a fold-of-cycles at around $Re \simeq 2337$, thus pairing with a shift–reflect saddle cycle of larger amplitude. This would be the saddle cycle approached by the right vertex. If collision of the torus with the two limit cycles were to occur simultaneously, as suggested by figure 25 and supported by the fold–pitchfork bifurcation scenario for maps (see Kuznetsov, Meijer & Van Veen (2004), for the closely related fold–flip bifurcation), a non-robust heteroclinic cycle would be created at Re_c leaving no attractors (see figure 1). No full description of the fold–pitchfork bifurcation for maps is available in the literature. It would correspond to the analysis of a 1:1 resonance (Kuznetsov 1995) in the presence of Z_2 symmetry, and the details are too intricate to be discussed here and will be treated elsewhere.
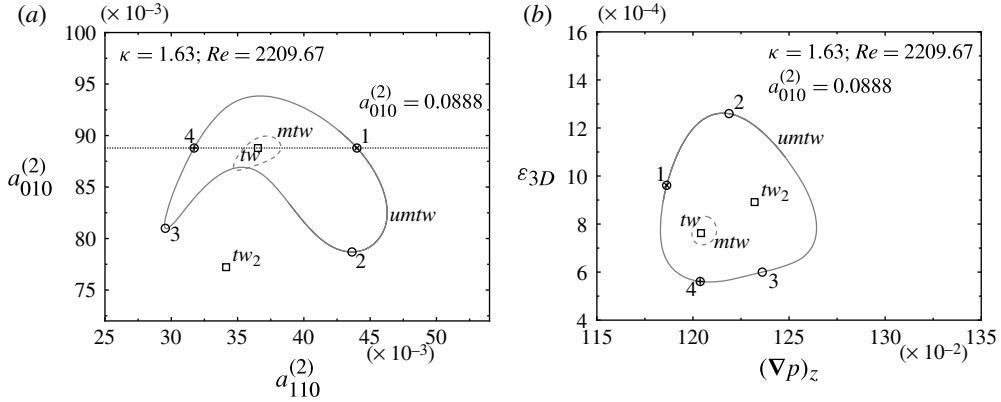
FIGURE 26. Phase map projections of an unstable modulated travelling wave (*umtw*) at $(\kappa, Re) = (1.63, 2209.67)$. (*a*) $a_{010}^{(2)}$ versus $a_{110}^{(2)}$. (*b*) Three-dimensional energy (ε_{3D}) versus axial pressure gradient ($(\nabla p)_z$). Symbols and labels as for figure 6. The modulated travelling wave *mtw* at the same parameter values is indicated by a dashed line. The Poincaré section is defined by $a_{010}^{(2)} = a_{010}^{(2)}(tw)$. Numbered circles correspond to snapshots in figure 28.

Using shift–reflect symmetry-restricted time-evolution and edge-tracking refinement (Skufca *et al.* 2006; Schneider *et al.* 2007), where the laminar and turbulent asymptotic states have been replaced by two clearly distinct paths towards the stable modulated wave, we have numerically computed the conjectured unstable modulated wave (*umtw*) with sufficient accuracy. It has a single real multiplier outside the unit circle corresponding to a shift–reflect eigenmode. Its location is perfectly congruent with a collision with the outer surface of the torus (right vertex) as the global bifurcation point is approached (see figure 25).

Inspection of the multipliers of *mtw* shows that the branch effectively experiences a fold-of-cycles (a shift–reflect real multiplier crosses the unit circle) and that *umtw* belongs precisely to the saddle branch created at the fold as schematically outlined in figure 1.

Figure 26 shows two alternative axial-drift-independent phase map projections of the unstable modulated travelling wave solution at $(\kappa, Re) = (1.63, 2209.67)$, close to the bifurcation point. It is a straightforward observation to identify *mtw* and *umtw* as bounding solutions for the asymptotic shift–reflect projection of the doubly modulated wave m^2sw as it approaches the bifurcation point (compare the three solutions in figures 24 and 25), and especially *umtw*, since *mtw* seems to be affected by manifold tangles. This correspondence gets even clearer when comparing figures 26(*b*) and 14(*b*). The projection of the doubly modulated wave seems to grow in the region bounded by *mtw* at the inside and *umtw* at the outside, the heteroclinic bifurcation corresponding to the simultaneous collision with both modulated waves.

The time-evolution of *umtw* is characterized in figure 27(*a*) through the representation of the axial drift speed (c_z, black line) and the mean axial pressure gradient ($(\nabla p)_z$, grey line) time-series along a full period of the solution. Comparing the time signals with those for *mtw* in figure 7(*a*), it becomes relatively clear that *umtw* results from an amplification of *mtw* once it has gone unstable at the fold. The Fourier transform of the energy contained in non-axisymmetric streamwise dependent modes (ε_{3D}) are plotted in figure 27(*b*), with the time signal shown in the inset
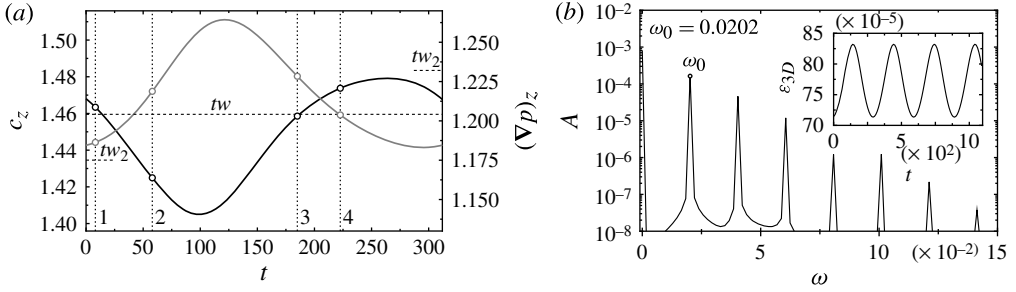
FIGURE 27. Unstable modulated travelling wave (*umtw*) at $(\kappa, Re) = (1.63, 2209.67)$. (*a*) Axial drift speed (c_z, black line) and axial pressure gradient ($(\nabla p)_z$, grey line) time-series. Dotted horizontal lines indicate the values for *tw* and *tw*$_2$ while numbered vertical lines and open circles indicate snapshots in figure 28. (*b*) Fourier transform of the non-axisymmetric streamwise dependent modal energy contents (ε_{3D}). Part of the time signal is plotted in the inset.
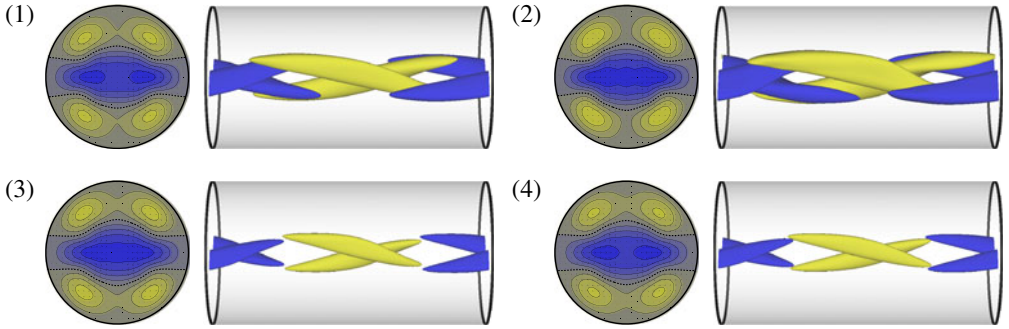

FIGURE 28. (Colour online) Unstable modulated travelling wave at $(\kappa, Re) = (1.63, 2209.67)$. Contour levels and colour coding as for figure 2. To avoid drift due to streamwise advection, snapshots are taken in a co-moving frame moving with the instantaneous advection speed from figure 27(*a*). The snapshots are indicated by open circles in figures 26 and 27(*a*). (1) $t = 8$; (2) $t = 58$; (3) $t = 184$; (4) $t = 222$.

frame. The resolution of the spectrum is not as good as for stable waves due to the difficulty in stabilizing an unstable wave for sufficiently long times, but it is sufficient to reveal a clear peak of angular frequency at $\omega_0 = 0.0202(4U/D)$, corresponding to a period $T_0 = 2\pi/\omega_0 = 311.2D/(4U)$. The *mtw* at the same parameter value has a slightly faster frequency, $\omega_0 = 0.0209\,(4U/D)$, corresponding to a shorter period $T_0 = 2\pi/\omega_0 = 299.9D/(4U)$.

To better support the relevance of the wave in the dynamics of the problem, a few snapshots (indicated in figures 26 and 27*a* with circles) of the flow field along a cycle are represented in figure 28 (see online movie). It is clear from the snapshots that the modulation is similar to but of slightly larger amplitude than the one seen for *mtw* at $Re = 2335$ (figure 8). Note also the similarity of snapshot (1) of figure 28 to the one in figure 19(*c*) for the approach to the shift–reflect space of the chaotic wave *cw* at $Re = 2215$. Taken together with the similarities of the phase map trajectories (see the winding of the trajectory near the shift–reflect subspace in figure 16) we conclude that this wave influences the dynamics even at *Re*-values beyond the global bifurcation.
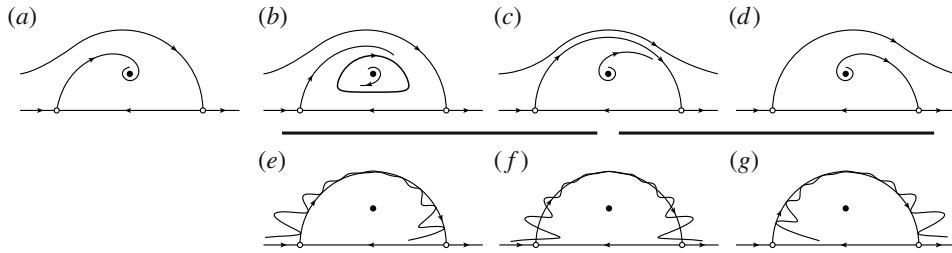
FIGURE 29. Schematic phase map representation on a Poincaré section of the formation and destruction of the chaotic set. (*a–d*) An approximating interpolated flow. (*e–g*) Sketch of the heteroclinic tangencies expected instead of (*c*). Phase maps are symmetric with respect to the horizontal axis, which represents the shift–reflect subspace, but only the upper half is shown.

The bifurcation scenario introduced in figure 1 is now schematically developed in figure 29(*a–d*). A stable modulated spiralling wave (filled circle) and two saddle modulated travelling waves (open circles on the horizontal axis, which represents the shift–reflect subspace) exist for sufficiently low *Re* (figure 29*a*). Strictly speaking, phase maps are symmetric with respect to the horizontal axis and a symmetry-related stable modulated spiralling wave should have been drawn. For simplicity, though, only the upper half is actually represented. In figure 29(*b*), the modulated spiralling wave has undergone a Neimark–Sacker bifurcation and a stable doubly modulated wave has been created (thick solid loop). This wave grows and collides with both modulated travelling waves simultaneously in figure 29(*c*), generating a heteroclinic cycle that leaves this phase space region open in figure 29(*d*), as observed for $Re \gtrsim 2225$.

The phase maps sketched correspond to approximating the Poincaré map by an interpolating flow. For the discrete map, heteroclinic cycles (*hc* in figure 1) will not generically arise. Instead, heteroclinic tangles and tangencies will typically occur, broadening the bifurcation point (or curve) into a wedge where complex dynamics and chaos are common feature. This is precisely what was observed in § 4. The appearance of chaotic waves, and the transition point discussed here, would then be related to the first heteroclinic tangency of the stable and unstable modulated wave manifolds (figure 29*e*). Chaotic waves exist for a finite range of the parameter (figure 29*f*) but end up disappearing and causing the phase space region they inhabited to open up (figure 29*g*, where the unstable manifold of *mtw* becomes externally tangent to the stable manifold of *umtw*), so that the flow can leave towards other regions. In the present case towards turbulent motion, as described above.

In the *Re*-range where chaotic waves exist, the manifolds' entanglement and interweaving is complicated by the presence of the travelling and spiralling wave solutions discussed in § 3. It is not possible with the tools at hand to gain a complete understanding of the role of relative equilibria and their manifolds in organizing the dynamics around the chaotic set. An example of the complex intermingling of manifolds is visible in figure 25 for $Re = 2209.6726$, where the reattachment to the remnants of the torus is sometimes accomplished along the unstable manifold of the travelling wave *tw* rather than along that of the modulated travelling wave *mtw*, as is clear from the alignment of black plus signs.

All things considered, the torus breakdown scenario involving a homoclinic or, rather, heteroclinic-cyclic connection, seems to be the most plausible. The logarithmic

fit of the period is supportive of this surmise, except that the fitting parameter λ needs to be reinterpreted and it is not clear as to which of either modulated waves it is related. The unstable multiplier associated to *mtw* has been measured and its value $\mu_{mtw} = 1.1265$ corresponds to an eigenvalue $\lambda = 3.972 \times 10^{-4}\,(4U/D)$, which is one order of magnitude smaller than the one resulting from the logarithmic fit. It could well be that the unstable manifold of the saddle cycle takes the lead as the unstable manifold of *mtw* loses strength in the presence of twisting and tangency. An indicator that this could be happening is the deformation of the bottom left corner of the cycle in figure 25, which seems to be adapting to the foldings of the tangle. Unfortunately, the unstable multiplier of *umtw* cannot by itself explain the divergence of the period, either. Its value, $\mu_{umtw} = 3.9549$, results in an eigenvalue $\lambda = 4.419 \times 10^{-3}\,(4U/D)$, which is larger, by a factor of two, than the parameter λ adjusted by the fit.

The bump observed for the fast frequency across the global bifurcation (figure 23*a*) would also be a consequence of this scenario. The fast frequency of m^2sw, which is initially governed by *msw*, would later be dictated by *mtw* and/or *umtw* as longer and longer times are spent in their vicinity. This follows from the asymptotic approach to the heteroclinic-cyclic connection. Once we cross into the region of *cw*, though, the influence is shared again by all three modulated waves.

6. Conclusion

We have studied the fate of upper-branch travelling waves of a shift–reflect symmetric family that belongs in the twofold azimuthally periodic subspace of pipe Poiseuille flow. The special stability properties of these waves, which are stable to perturbations within their azimuthal subspace in some regions of parameter space, allows us to track and identify the waves, and time-dependent solutions resulting from their ulterior destabilization, by direct time-evolution.

Despite the contorted continuation surfaces of these waves when analysed as a function of both axial wavenumber (κ) and Reynolds number (Re), a one-dimensional path at $\kappa = 1.63$ and varying Re suffices to unveil a multitude of increasingly complex solutions that are reported for the first time in pipe flow. Successive transitions to spiralling waves, modulated travelling waves, modulated spiralling waves and doubly modulated travelling waves have been reported along the way, and the arising solutions described to some extent, in order to exemplify the extreme richness and complexity of the problem, even within a given subspace. The bifurcation cascade has been shown to culminate in a torus breakdown, presumably following a cyclic heteroclinic connection of the stable and unstable manifolds of modulated travelling waves. The usual manifold entanglement and heteroclinic tangencies that occur in sufficiently high-dimensional (three or more) dynamical systems give the simplest explanation for the observed phenomenology, i.e. the formation of an attracting chaotic set upon torus breakdown and its subsequent dismantling at higher Re.

The rupture of the chaotic set no longer supports the existence of mildly chaotic waves, and the flow moves to other regions of phase space, namely twofold azimuthally periodic turbulence. Turbulence within the subspace is, as for a full-space pipe, sustained transiently by a chaotic saddle that already exists at lower Re and occupies a region of phase space far away from all solutions reported here (except possibly tw_3, sw_2 and sw_3). In this sense, it can be safely asserted that the chaotic set described here plays no significant role in the development of the phase space structures that comprise the turbulent saddle. This is clearly supported by figure 30,
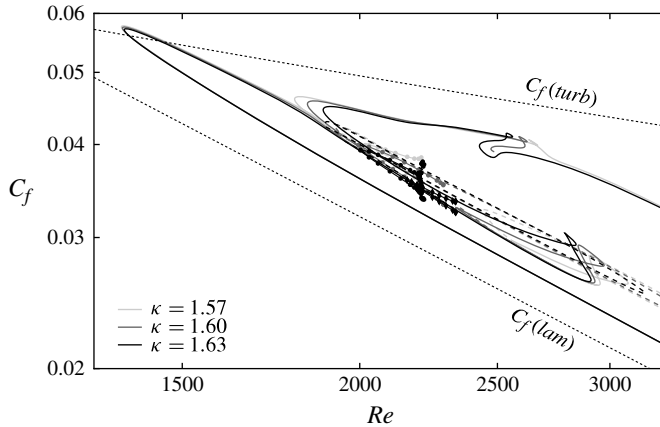
FIGURE 30. Friction factor (C_f) as a function of Re and κ (line shading as explained in the legend). Solid lines represent shift–reflect travelling waves, dashed lines are spiralling waves. Extrema of time-dependent travelling/spiralling solutions are marked as filled diamonds/circles. Turbulent ($C_f(turb)$, from the experimentally obtained log-law $1/\sqrt{C_f} = 2\log_{10}(Re\sqrt{C_f}) - 0.8$ – see Schlichting & Gersten (2000), p. 551) and laminar ($C_f(lam) = 64/Re$) friction factors are indicated by dotted lines.

where friction factor (C_f) is plotted as a function of Re. Laminar and turbulent typical friction factor values are indicated by dotted lines. It is evident that, while lower-branch waves approach laminar values and upper-branch waves are close to turbulent friction factors, all other solutions reported in the present study are confined in a narrow strip halfway between laminarity and turbulence. Unlike the homoclinic loop of van Veen & Kawahara (2011), the heteroclinic-cyclic connection presented here is not responsible for turbulent bursts.

It is nevertheless plausible that similar bifurcation cascades might take place in other subspaces for which our simulation tools are currently incapable of overcoming the effects of higher-dimensional unstable manifolds. Newton–Krylov methods for the computation, continuation and stability analysis of unstable complex solutions of the Navier–Stokes equations, such as relative periodic orbits (Viswanath 2006) or tori (Sanchez *et al.* 2010), would help broaden the scope of this type of study to include these other subspaces. Some of the chaotic sets thus generated could well go into the formation of a turbulent saddle, although global bifurcations involving several subspaces simultaneously may well complicate the picture even further.

Extending the current analysis to varying κ could help us to better understand the global bifurcation leading to chaos. In particular, continuing time-dependent solutions to larger κ, preferably along unstable branches where possible, would help clarify the connections among modulated travelling and spiralling waves, and possibly completely unfold the fold–pitchfork bifurcation of maps advanced here to account for the appearance of chaotic waves.

Further, the direct study of twofold azimuthally symmetric turbulence, which in itself involves great complexity, may yield results that can help us gain intuition into what may be happening in fully fledged turbulence. The twofold azimuthally symmetric subspace has already proved to be a particularly accessible terrain in this respect.
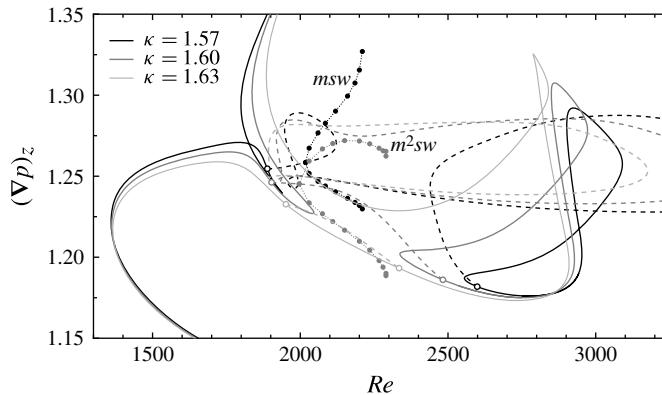
FIGURE 31. Mean axial pressure gradient $((\nabla p)_z)$ as a function of *Re* for $\kappa = 1.57$, 1.60. Symbols as for figure 3. The case $\kappa = 1.63$ of figure 3 is shown in light grey for comparison.

Supplementary movies

Supplementary movies are available at http://dx.doi.org/10.1017/jfm.2012.326.

Appendix A. Axial wavenumber effects

Varying κ away from $\kappa = 1.63$ changes the bifurcation cascade described. In this appendix we briefly consider some of the ways in which the scenario is modified for longer waves. For shorter wavelengths, the bifurcation of modulated waves bypasses the existence of travelling waves.

The behaviour of upper-branch travelling waves depends strongly on κ. This is apparent from figure 31. At these lower κ, the continuation curve splits into two, adding two extra saddle-node points and leaving an island of solutions at moderate *Re*. Figure 32 shows a close-up of the parameter region where this topological change takes place. It becomes clear in figure 32(*a*) that for $\kappa \lesssim 1.607$, the segments of the continuation curve corresponding to *tw* and tw_2 collide and produce a gap in *Re* where the multiplicity of solutions is reduced to just two. Waves *tw* and tw_2 at $(\kappa, Re) = (1.63, 2215)$ (figure 2*b,c*) already look much alike and, indeed, collide in a saddle-node point and disappear as κ is reduced, leaving tw_0 and tw_3 (figure 2*a,d*) as the only surviving members of the family.

The disappearance of *tw* for $\kappa \lesssim 1.607$ in a wide range of *Re* does not preclude, in principle, the bifurcation scenario exemplified for $\kappa = 1.63$. The bifurcation cascade is still possible as long as the branch of spiralling waves *sw* persists.

While this holds true for $\kappa = 1.60$ (grey dashed line in figure 31), it is no longer the case for the lower $\kappa = 1.57$ shown (black dashed line). The *Re*-continuation curve of spiralling waves starts at a pitchfork point, exhibits a series of bends and twists, and ends up branching back with middle-branch travelling waves in a second pitchfork. In this way, the spiralling waves still bridge the *Re*-gap left by middle-branch travelling waves described above, but a new gap is created for which no *sw* solutions exist. The
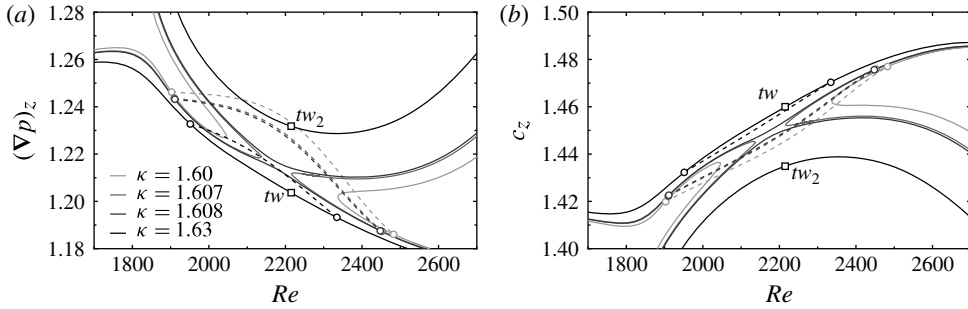
FIGURE 32. Detail near $(\kappa, Re) \sim (1.61, 2200)$ highlighting the change in behaviour of the continuation curves. Solid lines represent travelling waves (darker for increasing κ) whereas dashed lines correspond to spiralling waves (*sw*). Lower-middle branch (*tw*) and upper-middle branch (tw_2) waves are indicated by squares. Open circles denote pitchfork bifurcations. (*a*) Mean axial pressure gradient $(\nabla p)_z$ and (*b*) axial advection speed (c_z), as a function of Re.
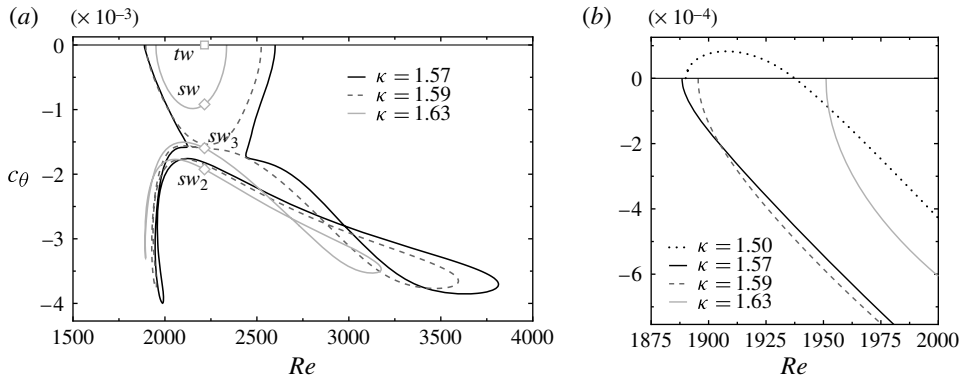

FIGURE 33. (*a*) Rotation drift speed (c_θ) as a function of Re and κ (shading) for spiralling waves. Shift–reflect travelling waves collapse on the *x*-axis. Symbols and labels as for figure 3. (*b*) Detail of the bifurcating point including lower κ-curves.

gap is clearly exposed in figure 33(*a*), where the rotation speed of the waves is plotted against Re.

To recover the two disconnected branches of spiralling solutions shown to exist for $\kappa = 1.63$, some bifurcation must have taken place in between. The topological change occurs for $\kappa \gtrsim 1.59$ (dashed curve in figure 33*a*), at which point the long continuation curve splits in two, leaving a disconnected island of strongly spiralling waves ($sw_{2,3}$) and an uneventful curve (*sw*) connecting at both ends with the travelling wave family.

It has already been pointed out that spiralling waves that break a left–right symmetry, here in the form of a shift–reflect symmetry, appear in symmetry-related pairs that rotate either clockwise or anticlockwise with opposite rotation speeds. This is a general remark, but the loss of symmetry does not preclude the existence of non-robust asymmetric waves that balance the azimuthal driving force and, consequently, do not rotate. As is the case for some helical waves in pipe flow (Pringle & Kerswell 2007), non-shift–reflect waves exist whose rotation rate cancels exactly. This is exemplified for $\kappa = 1.50$ (dotted line) in figure 33(*b*), where a branch of
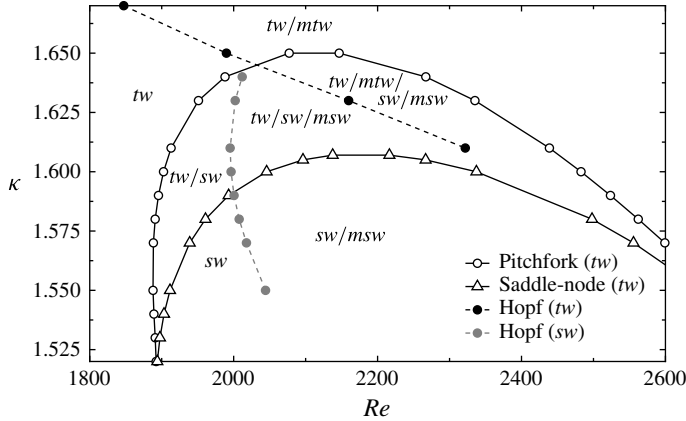
FIGURE 34. Bifurcation curves on (Re, κ)-parameter space as explained in the legend. Regions of existence of travelling, spiralling, modulated travelling and modulated spiralling waves are labelled *tw*, *sw*, *mtw* and *msw*, respectively.

spiralling waves first appears with anticlockwise rotation that only for higher Reynolds numbers switches to the clockwise rotation that characterizes all other spiralling waves continued in the plot. As the rotation speed crosses zero, two mutually symmetric spiralling waves switch the direction of rotation. Since this crossing happens for a specific value of the system parameters it is a non-robust, non-generic phenomenon.

The bifurcation cascade described in the main text may even outlast the disappearance of the *sw* branch, as long as the branch of modulated waves *msw* is still created, as is the case for $\kappa = 1.57$ (see figure 31). The stability analysis of § 3.3 has been broadened by varying κ and Re together in order to extend the bifurcation points into bifurcation curves in a thorough exploration of the topology of parameter space.

Tracks of the bifurcation points from figure 5 in (Re, κ)-parameter space are shown in figure 34. A saddle-node bifurcation curve (solid line with triangles), only present for $\kappa \lesssim 1.607$, delimits a region where no middle-branch travelling waves exist, as described above and illustrated in figure 32. A pitchfork bifurcation curve (solid line with open circles) delimits the region of existence of lower-branch spiralling waves (*sw*). Middle- and upper-branch spiralling waves can extend beyond this region and actually do so as shown in figure 33. In the region where travelling waves exist, modulated travelling waves that preserve the shift–reflect symmetry appear along a Hopf line (black dashed line with filled circles). As the travelling wave Hopf line crosses into the region of existence of spiralling waves, another Hopf line (grey dashed line with filled circles), duplicated from the original but related to the destabilization of spiralling waves, starts running on their continuation surface. The supercritical nature described for $\kappa = 1.63$ is preserved along the whole extent of both Hopf lines, so that modulated waves only exist to their right.

In principle, the presence of the Hopf line of *sw* for $\kappa < 1.59$ is indicative that the bifurcation cascade can still take place, even if *tw* and *sw* have ceased to exist in a vast *Re*-range.

The bifurcation cascade indeed starts for these lower values of κ, but it does not reach the point where a chaotic set is created. At the lower wavenumber explored ($\kappa = 1.57$, dark solid circles in figure 31), the modulated spiralling waves branch
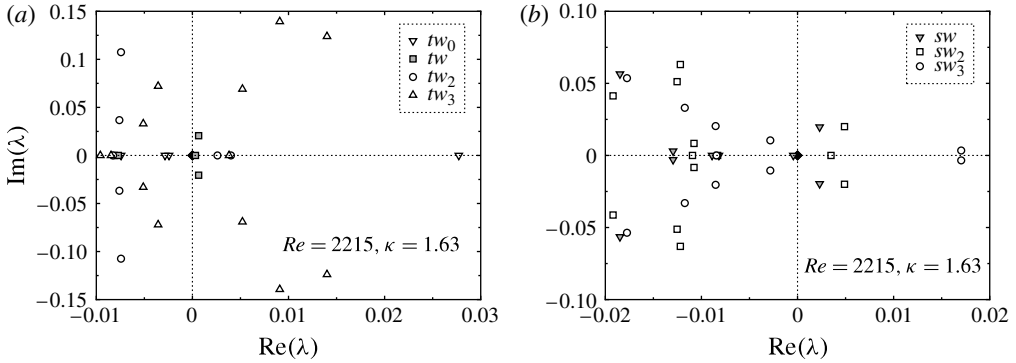
FIGURE 35. Spectra of (*a*) travelling and (*b*) spiralling waves at $(Re, \kappa) = (2215, 1.63)$ as indicated in figure 3(*a*). Eigenvalues are coded as explained in the legend. The black diamond at the origin represents degenerate eigenmodes corresponding to infinitesimal translation and rotation of the waves.

seems to undergo a fold-of-cycles. The bifurcation scenario presented in figure 1 is not applicable to this lower κ. For intermediate wavenumbers ($\kappa = 1.60$, grey solid circles) doubly modulated waves develop, but their track is lost shortly after bifurcation in what seems to be a fold-of-tori, which will not be pursued here. At this κ, the bifurcation diagram of figure 1 would be complicated in ways that make it inaccessible.

For shorter waves ($\kappa > 1.63$), it is plausible that the appearance of *msw* bypasses the existence of *sw* by bifurcating directly from *mtw* in a pitchfork of cycles. This is precisely what is to be expected in the fold–pitchfork bifurcation scenario for maps.

Appendix B. Eigenmodes of travelling and spiralling waves

Most of the transitions undergone by travelling and spiralling waves result in states that are unstable at onset and therefore not accessible through time-evolution. Nonetheless, a careful analysis of their eigenmodes gives some hints as to how the waves are interconnected in phase space and what these bifurcating solutions may look like.

Figure 35(*a,b*) depicts the eigenspectra at $(Re, \kappa) = (2215, 1.63)$ of all four coexisting shift–reflect travelling waves and of all three spiralling waves, respectively. Apart from the degenerate eigenmodes corresponding to infinitesimal translations and rotations shared by all waves (filled black diamond at the origin), tw_0 (downward-pointing triangles in figure 35*a*) has a single unstable real eigenmode, a relict from the saddle-node at which the wave was created together with *tw*. The upper-branch wave, tw_3 (upward-pointing triangles), exhibits, after a long sequence of destabilizations and restabilizations that go beyond the scope of this study, a total of seven unstable directions: an unstable shift–reflect symmetric complex pair, and an unstable real eigenvalue and two complex pairs pointing out of the symmetry subspace. As shown in figure 5, *tw* has both an unstable real eigenvalue and an unstable complex pair at $Re = 2215$. The unstable real eigenmode of *tw* (shaded squares) is shift–reflect antisymmetric and points in the direction of *sw*. Its symmetry-breaking nature is clear from figure 36(*a*), where mean axial velocity contours are shown to be exactly antisymmetric and axial vorticity has a dominant sign, a feature that is imprinted upon *sw*. Of course, shooting in the opposite direction (changing the sign of the eigenmode),
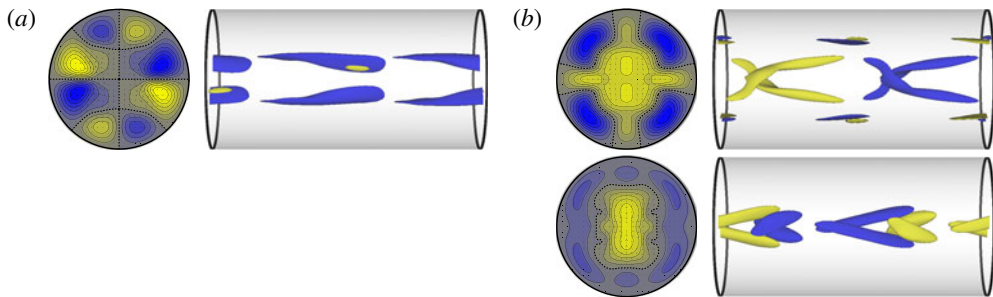
FIGURE 36. (Colour online) Unstable eigenmodes of *tw* (see figure 35*a*) at $(\kappa, Re) = (1.63, 2215)$. Averaged cross-sectional axial velocity contours with in-plane velocity vectors and three-dimensional isosurfaces of axial vorticity (blue/dark for negative, yellow/light for positive). (*a*) Symmetry-breaking real eigenmode. (*b*) Real (top) and imaginary (bottom) parts of the symmetry-preserving unstable complex pair. Axial vorticity has been scaled $(\omega_z(\text{Im}) = 5\omega_z(\text{Re}))$ to aid visualization.

the shift–reflect-conjugate version of *sw* can be found. The leading complex pair of *tw* are shift–reflect symmetric and point in the direction of an invariant unstable manifold leading to the modulated travelling wave described in § 4.1. The real and imaginary parts of the eigenmode are shown in figure 36(*b*), where axial vorticity isosurfaces of the real part are rescaled by a factor of 5 to make real and imaginary parts of comparable magnitude. The shift–reflect character of the complex pair is clear from the figure. The upper-middle-branch wave tw_2 (circles) has an unstable shift–reflect symmetric real eigenvalue (figure 37*a*), presumably left from the saddle-node at which the wave merges with *tw* at higher *Re*, and an additional symmetry-breaking real eigenvalue inherited from *tw*. The associated eigenmode is shown in figure 37(*b*) and preserves some of the features of the unstable symmetry-breaking eigenmode of *tw*, such as the streak layout and the signature of the vortical structure, although their respective symmetry-breaking unstable manifolds have deformed and may already lead to different phase space regions.

Spiralling waves sw_2 (squares in figure 35*b*) and sw_3 (circles) exhibit an unstable real eigenvalue together with a complex pair and just a complex pair, respectively. The real unstable eigenvalue of middle-branch sw_2 is the remnant of saddle-node bifurcations relating the wave with *sw* and sw_3 at other values of *Re* and κ. The unstable manifold defined by it is therefore expected to lead to *sw* and sw_3 at either side of sw_2. The complex pair, shared by all three spiralling waves, is at the origin of the branch of modulated spiralling waves branching off *sw* and described in § 4.2. This eigenmode is represented in figure 37(*c*). This complex pair of eigenvectors is remarkably similar to that of *tw* (figure 36*b*). They look alike in all respects except that the latter preserves the shift–reflect symmetry while the former does not. The fact that both Hopf lines of figure 34 coalesce in a single point in (κ, Re) parameter space is not a coincidence. In fact, it is to be expected that modulated travelling waves and modulated spiralling waves are related by a pitchfork bifurcation of a symmetric fixed cycle (Kuznetsov 1995).

All unstable eigenmodes of figure 35 are reported in the last two columns of table 1, either in $ev \in S$ or $ev \in \bar{S}$, depending on whether they do or do not belong to the shift–reflect subspace, respectively.
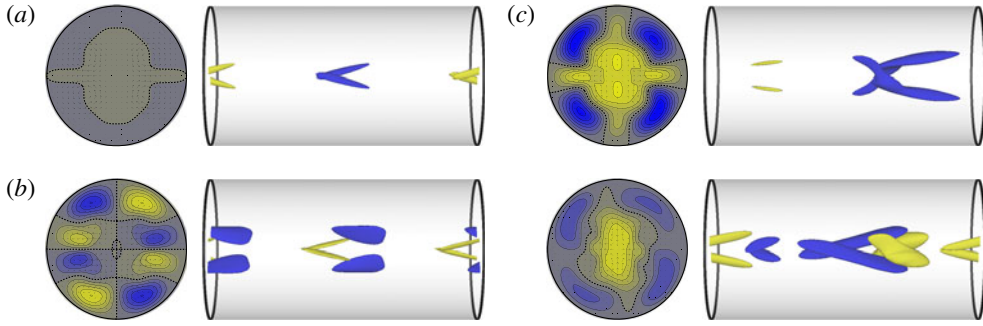
FIGURE 37. (Colour online) Unstable eigenmodes of tw_2 (see figure 35a) and sw (see figure 35b) at $(\kappa, Re) = (1.63, 2215)$. (a) Symmetry-preserving real eigenvector of tw_2. (b) Symmetry-breaking real eigenvector of tw_2. (c) Real (top) and imaginary (bottom) parts of the unstable complex pair of sw. Averaged cross-sectional axial velocity contours with in-plane velocity vectors and three-dimensional isosurfaces of axial vorticity (blue/dark for negative, yellow/light for positive). Axial vorticity has been scaled ($\omega_z(\text{Im}) = 5\omega_z(\text{Re})$) to aid visualization.
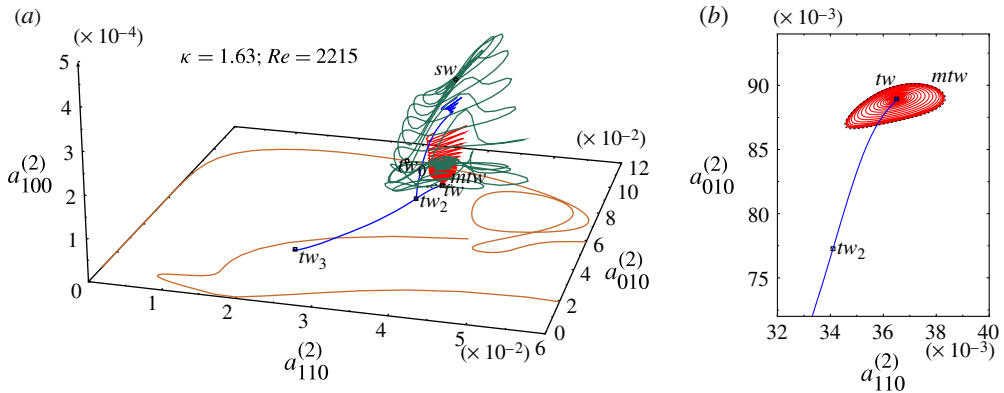

FIGURE 38. (Colour online) (a) Phase map projections of the unstable manifolds of tw (red), sw (green), tw_0 (orange) and tw_2 (blue) at $(\kappa, Re) = (1.63, 2209.67)$. Symbols and labels as for figure 9. (b) Detail of the shift–reflect vicinity of tw.

Figure 38 illustrates the unstable manifolds of some of the travelling and spiralling waves, showing some of the connections hinted at by the eigenmodes. The unstable manifold of the lower-branch wave tw_0 (orange), leads to the basic flow on one side and towards the vicinity of tw_3 and shift–reflect turbulence on the other. The wave tw_2 separates the basins of attraction of tw and tw_3, as clearly shown by the direct connecting shift–reflect manifolds (blue). Out of the shift–reflect plane, the only unstable manifold of tw_2 seems to lead towards sw, although after a while the computation starts to spiral due to the presence of a modulational instability. It is the instability governed by the complex pair shared by both tw and sw. While in the case of tw the manifold spirals until convergence on mtw (red), for sw it gradually converges onto cw (green). Finally, the shift–reflect-orthogonal unstable eigenmode of tw points towards sw, but the modulational instability is already much stronger and the

computation soon bends the manifold towards *cw*. The unstable manifolds leaving tw_3, sw_2 and sw_3 (not shown) all lead either to turbulence or to *cw* in a non-trivial way.

REFERENCES

ANISCHENKO, V. S., SAFONOVA, M. A. & CHUA, L. O. 1993 Confirmation of the Afraimovich–Shilnikov torus-breakdown theorem via a torus circuit. *IEEE Trans. Cir. Sys.* **40** (11), 792–800.

AVILA, K., MOXEY, D., DE LOZAR, A., AVILA, M. & HOF, B. 2011 The onset of turbulence in pipe flow. *Science* **333** (6039), 192–196.

AVILA, M., WILLIS, A. P. & HOF, B. 2010 On the transient nature of localized pipe flow turbulence. *J. Fluid Mech.* **646**, 127–136.

BOBERG, L. & BROSA, U. 1988 Onset of turbulence in a pipe. *Z. Naturforsch.* A **43**, 697–726.

BROSA, U. & GROSSMANN, S. 1999 Minimum description of the onset of pipe turbulence. *Eur. Phys. J.* B **9** (2), 343–354.

CHENCINER, A. & IOOSS, G. 1979 Bifurcation of invariant torus. *Arch. Rat. Mech. Anal.* **69** (2), 109–198.

CHOSSAT, P. & LAUTERBACH, R. 2000 *Methods in Equivariant Bifurcations and Dynamical Systems*. World Scientific.

CRAWFORD, J. D. & KNOBLOCH, E. 1991 Symmetry and symmetry-breaking bifurcations in fluid dynamics. *Annu. Rev. Fluid Mech.* **23**, 341–387.

DARBYSHIRE, A. G. & MULLIN, T. 1995 Transition to turbulence in constant-mass-flux pipe flow. *J. Fluid Mech.* **289**, 83–114.

DUGUET, Y., PRINGLE, C. C. T. & KERSWELL, R. R. 2008 Relative periodic orbits in transitional pipe flow. *Phys. Fluids* **20** (11), 114102.

DUGUET, Y., WILLIS, A. P. & KERSWELL, R. R. 2008 Transition in pipe flow: the saddle structure on the boundary of turbulence. *J. Fluid Mech.* **613**, 255–274.

ECKHARDT, B. 2009 Introduction. Turbulence transition in pipe flow: 125th anniversary of the publication of Reynolds' paper. *Phil. Trans. R. Soc. Lond.* A **367** (1888), 449–455.

ECKHARDT, B., FAISST, H., SCHMIEGEL, A. & SCHNEIDER, T. M. 2008 Dynamical systems and the transition to turbulence in linearly stable shear flows. *Phil. Trans. R. Soc. Lond.* A **366**, 1297–1315.

ECKHARDT, B., SCHNEIDER, T. M., HOF, B. & WESTERWEEL, J. 2007 Turbulence transition in pipe flow. *Annu. Rev. Fluid Mech.* **39**, 447–468.

EHRENSTEIN, U. & KOCH, W. 1991 Three-dimensional wave-like equilibrium states in plane Poiseuille flow. *J. Fluid Mech.* **228**, 111–148.

FAISST, H. & ECKHARDT, B. 2003 Travelling waves in pipe flow. *Phys. Rev. Lett.* **91** (22), 224502.

GASPARD, P. 1990 Measurement of the instability rate of a far-from-equilibrium steady state at an infinite period bifurcation. *J. Phys. Chem.* **94** (1), 1–3.

GIBSON, J. F., HALCROW, J. & CVITANOVIĆ, P. 2008 Visualizing the geometry of state space in plane Couette flow. *J. Fluid Mech.* **611**, 107–130.

GIBSON, J. F., HALCROW, J. & CVITANOVIĆ, P. 2009 Equilibrium and travelling-wave solutions of plane Couette flow. *J. Fluid Mech.* **638**, 243–266.

GOLUBITSKY, M., LEBLANC, V. G. & MELBOURNE, I. 2000 Hopf bifurcation from rotating waves and patterns in physical space. *J. Nonlinear Sci.* **10** (1), 69–101.

GOLUBITSKY, M., STEWART, I. & SCHAEFFER, D. G. 1988 Singularities and groups in bifurcation theory, vol. 2. In *Applied Mathematical Sciences*, vol. 69. Springer.

GROSSMANN, S. 2000 The onset of shear flow turbulence. *Rev. Mod. Phys.* **72** (2), 603–618.

HOF, B., VAN DOORNE, C. W. H., WESTERWEEL, J., NIEUWSTADT, F. T. M., FAISST, H., ECKHARDT, B., WEDIN, H., KERSWELL, R. R. & WALEFFE, F. 2004 Experimental observation of nonlinear travelling waves in turbulent pipe flow. *Science* **305** (5690), 1594–1598.

HOF, B., SCHNEIDER, T. M., WESTERWEEL, J. & ECKHARDT, B. 2006 Finite lifetime of turbulence in shear flows. *Nature* **443** (7107), 59–62.

KERSWELL, R. R. & TUTTY, O. R. 2007 Recurrence of travelling waves in transitional pipe flow. *J. Fluid Mech.* **584**, 69–102.

KRUPA, M. 1990 Bifurcations of relative equilibria. *SIAM J. Math. Anal.* **21** (6), 1453–1486.

KUZNETSOV, Y. A. 1995 *Elements of Applied Bifurcation Theory*, third edition. Springer.

KUZNETSOV, Y. A., MEIJER, H. G. E. & VAN VEEN, L. 2004 The fold-flip bifurcation. *Intl J. Bifurcation Chaos* **14** (7), 2253–2282.

LANDAU, L. 1944 On the problem of turbulence. *Dokl. Akad. Nauk SSSR* **44**, 339–342.

MARQUES, F., LOPEZ, J. M. & SHEN, J. 2001 A periodically forced flow displaying symmetry breaking via a three-tori gluing bifurcation and two-tori resonances. *Physica* D **156**, 81–97.

MECA, E., MERCADER, I., BATISTE, O. & RAMÍREZ-PISCINA, L. 2004 Blue sky catastrophe in double-diffusive convection. *Phys. Rev. Lett.* **92** (23), 234501.

MELLIBOVSKY, F. & ECKHARDT, B. 2011 Takens–Bogdanov bifurcation of travelling wave solutions in pipe flow. *J. Fluid Mech.* **670**, 96–129.

MELLIBOVSKY, F. & MESEGUER, A. 2009 Critical threshold in pipe flow transition. *Phil. Trans. R. Soc. Lond.* A **367** (1888), 545–560.

MESEGUER, A. & MELLIBOVSKY, F. 2007 On a solenoidal Fourier–Chebyshev spectral method for stability analysis of the Hagen–Poiseuille flow. *Appl. Numer. Math.* **57**, 920–938.

MESEGUER, A. & TREFETHEN, L. N. 2003 Linearized pipe flow to Reynolds number 10^7. *J. Comput. Phys.* **186**, 178–197.

NAGATA, M. 1997 Three-dimensional travelling-wave solutions in plane Couette flow. *Phys. Rev.* E **55** (2), 2023–2025.

NEWHOUSE, S., RUELLE, D. & TAKENS, F. 1978 Occurrence of strange axiom A attractors near quasi-periodic flows on T^m, $m = 3$. *Commun. Math. Phys.* **64**, 35–40.

PFENNIGER, W. 1961 Boundary Layer and Flow Control. (ed. G. V. Lachman). pp. 970–980. Pergamon.

PRINGLE, C. C. T., DUGUET, Y. & KERSWELL, R. R. 2009 Highly symmetric travelling waves in pipe flow. *Phil. Trans. R. Soc. Lond.* A **367** (1888), 457–472.

PRINGLE, C. C. T. & KERSWELL, R. R. 2007 Asymmetric, helical, and mirror-symmetric travelling waves in pipe flow. *Phys. Rev. Lett.* **99** (7), 074502.

PUGH, J. D. & SAFFMAN, P. G. 1988 Two-dimensional superharmonic stability of finite-amplitude waves in plane Poiseuille flow. *J. Fluid Mech.* **194**, 295–307.

RAND, D. 1982 Dynamics and symmetry: predictions for modulated waves in rotating fluids. *Arch. Rat. Mech. Anal.* **79** (1), 1–37.

REYNOLDS, O. 1883 An experimental investigation of the circumstances which determine whether the motion of water shall be direct or sinuous and of the law of resistance in parallel channels. *Phil. Trans. R. Soc. Lond.* **174**, 935–982.

RUELLE, D. & TAKENS, F. 1971 On the nature of turbulence. *Commun. Math. Phys.* **20**, 167–192.

SANCHEZ, J., NET, M. & SIMO, C. 2010 Computation of invariant tori by Newton–Krylov methods in large-scale dissipative systems. *Physica* D **239**, 123–133.

SCHLICHTING, H. & GERSTEN, K. 2000 *Boundary-Layer Theory*, eighth edition. Springer.

SCHMID, P. J. & HENNINGSON, D. S. 1994 Optimal energy growth in Hagen–Poiseuille flow. *J. Fluid Mech.* **277**, 197–225.

SCHNEIDER, T. M. & ECKHARDT, B. 2009 Edge states intermediate between laminar and turbulent dynamics in pipe flow. *Phil. Trans. R. Soc. Lond.* A **367** (1888), 577–587.

SCHNEIDER, T. M., ECKHARDT, B. & VOLLMER, J. 2007 Statistical analysis of coherent structures in transitional pipe flow. *Phys. Rev.* E **75** (6), 066313.

SCHNEIDER, T. M., ECKHARDT, B. & YORKE, J. A. 2007 Turbulence transition and edge of chaos in pipe flow. *Phys. Rev. Lett.* **99** (3), 034502.

SHAN, H., MA, B., ZHANG, Z. & NIEUWSTADT, F. T. M. 1999 On the spatial evolution of a wall-imposed periodic disturbance in pipe Poiseuille flow at $Re = 3000$. Part 1. Subcritical disturbance. *J. Fluid Mech.* **398**, 181–224.

SKUFCA, J. D., YORKE, J. A. & ECKHARDT, B. 2006 Edge of chaos in a parallel shear flow. *Phys. Rev. Lett.* **96** (17), 174101.

SOIBELMAN, I. & MEIRON, D. I. 1991 Finite-amplitude bifurcations in plane Poiseuille flow: two-dimensional Hopf bifurcation. *J. Fluid Mech.* **229**, 389–416.

STROGATZ, S. H. 1994 *Nonlinear Dynamics and Chaos*. Westview.

VAN VEEN, L. & KAWAHARA, G. 2011 Homoclinic tangle on the edge of shear turbulence. *Phys. Rev. Lett.* **107** (11), 114501.

VISWANATH, D. 2006 Recurrent motions within plane-Couette turbulence. *J. Fluid Mech.* **580**, 339–358.

VISWANATH, D. 2009 The critical layer in pipe flow at high Reynolds number. *Phil. Trans. R. Soc. Lond.* A **367** (1888), 561–576.

VOLLMER, J., SCHNEIDER, T. M. & ECKHARDT, B. 2009 Basin boundary, edge of chaos and edge state in a two-dimensional model. *New J. Phys.* **11**, 013040.

WANG, J., GIBSON, J. & WALEFFE, F. 2007 Lower branch coherent states in shear flows: transition and control. *Phys. Rev. Lett.* **98** (20), 204501.

WEDIN, H. & KERSWELL, R. R. 2004 Exact coherent structures in pipe flow: travelling wave solutions. *J. Fluid Mech.* **508**, 333–371.

WILLIS, A. P. & KERSWELL, R. R. 2008 Coherent structures in localized and global pipe turbulence. *Phys. Rev. Lett.* **100** (12).

WYGNANSKI, I. J. & CHAMPAGNE, F. H. 1973 On transition in a pipe. Part 1. The origin of puffs and slugs and the flow in a turbulent slug. *J. Fluid Mech.* **59**, 281–335.

WYGNANSKI, I. J., SOKOLOV, M. & FRIEDMAN, D. 1975 On transition in a pipe. Part 2. The equilibrium puff. *J. Fluid Mech.* **69**, 283–304.

ZIKANOV, O. Y. 1996 On the instability of pipe Poiseuille flow. *Phys. Fluids* **8** (11), 2923–2932.